MYC overrides HIF to regulate proliferating primary cell metabolism in hypoxia

Courtney A. Copeland[1,2], Benjamin A. Olenchock[1,2], David R. Ziehr[1,3,2], Sarah McGarrity[1,2,4], Kevin Leahy[1,2], Jamey D. Young[5], Joseph Loscalzo[1,2], and William M. Oldham[1,2,‡]

[1] Department of Medicine, Brigham and Women's Hospital, Boston, MA 02115, U.S.A.

[2] Department of Medicine, Harvard Medical School, Boston, MA 02115, U.S.A.

[3] Department of Medicine, Massachusetts General Hospital, Boston, MA, 02114 U.S.A.

[4] Center for Systems Biology, School of Health Sciences, University of Iceland, Reykjavik, Iceland

[5] Departments of Chemical & Biomolecular Engineering and Molecular Physiology & Biophysics, Vanderbilt University, Nashville, TN 37240, U.S.A.

[‡] Correspondence: William M. Oldham <woldham@bwh.harvard.edu>

ABSTRACT

Hypoxia requires metabolic adaptations to sustain energetically demanding cellular activities. While the metabolic consequences of hypoxia have been studied extensively in cancer cell models, comparatively little is known about the metabolic response of primary cells to hypoxia. We performed metabolic flux analyses of proliferating human lung fibroblasts and pulmonary artery smooth muscle cells in hypoxia. Unexpectedly, hypoxia decreased glycolytic flux despite activation of hypoxia-inducible factor (HIF) and increased glycolytic enzyme expression. Pharmacologic activation of HIF with the prolyl hydroxylase (PHD) inhibitor molidustat in normoxia did increase glycolytic flux, but hypoxia abrogated this effect. Multi-omic profiling revealed distinct molecular responses to hypoxia and pharmacologic PHD inhibition and suggested a critical role for MYC in modulating the HIF response in hypoxia. MYC knockdown in hypoxia increased lactate efflux, while MYC overexpression in normoxia blunted the effects of molidustat treatment. Together, these data suggest that other factors, notably MYC, supersede the anticipated effects of HIF-dependent up-regulation of glycolytic gene expression on glycolytic flux in hypoxic proliferating primary cells.

KEYWORDS

hypoxia / metabolic flux analysis / hypoxia-inducible factor / prolyl hydroxylase / MYC

INTRODUCTION

Cellular responses to hypoxia propel many physiologic and pathologic processes from wound healing and angiogenesis to vascular remodeling and fibrosis (Semenza, 2012; Lee *et al*, 2019a). These activities require cells to continue energetically demanding tasks, such as macromolecular biosynthesis and proliferation, despite limited oxygen availability. Since respiration is the most efficient way for cells to produce energy, cell metabolism must adapt to meet energetic needs when oxygen supply is limiting. Understanding how these metabolic adaptations sustain critical cellular processes in hypoxia is fundamentally important to our understanding of human health and disease.

Cells typically respond to hypoxia by shifting energy production away from respiration and toward glycolysis. This response is mediated primarily by stabilization of the hypoxia-inducible transcription factor 1α (HIF-1α). HIF-1α activates the transcription of glucose transporters, glycolytic enzymes, lactate dehydrogenase, and pyruvate dehydrogenase kinase, while decreasing the expression of tricarboxylic acid (TCA) cycle and electron transport chain enzymes (Semenza, 2012; Lee *et al*, 2020). Although HIF-1α is constitutively expressed, it is hydroxylated by prolyl hydroxylase enzymes (PHDs) in normoxia and targeted for proteasomal degradation. PHDs are the principal oxygen sensors in metazoan cells (Kaelin & Ratcliffe, 2008). PHDs are α-ketoglutarate-dependent dioxygenase enzymes that require molecular oxygen for their enzymatic activity. When oxygen tension falls, PHD activity decreases, leading to HIF-1α stabilization and activation of its associated transcriptional program. Overall, this transcriptional program should increase glycolytic capacity and divert glucose-derived pyruvate from oxidative phosphorylation toward lactate fermentation to maintain glycolytic ATP production.

In addition to metabolic changes designed to maintain energy supply, hypoxic cells also reduce energy demand through down-regulation of Na^+/K^+-ATPase, slowing protein translation, and decreasing cell proliferation (Wheaton & Chandel, 2011; Hubbi & Semenza, 2015). In particular, HIF-1α decreases cell proliferation by activating cyclin-dependent kinase inhibitor expression, inhibiting cell-cycle checkpoint progression (Gardner *et al*, 2001), and antagonizing pro-proliferative MYC signaling (Koshiji *et al*, 2004). Despite these canonical effects of HIF-1α activation, there are many examples where cells continue to proliferate despite hypoxic stress, including cancer cells, stem cells, and lung vascular cells (Hubbi & Semenza, 2015). How these cells meet the metabolic needs of sustained proliferation in hypoxia and how these adaptations are regulated are active areas of investigation (Jain *et al*, 2020; Oldham *et al*, 2015; Lee *et al*, 2020). Since hypoxia is a prominent feature of cancer biology as tumor growth outstrips blood supply, most detailed metabolic studies of hypoxic cell

59 metabolism have used tumor cell models, yielding important insights into the metabolic pathobiology of cancer
60 (Wise *et al*, 2011; Metallo *et al*, 2011; Melendez-Rodriguez *et al*, 2019; Garcia-Bermudez *et al*, 2018; Lee *et al*,
61 2019b; Jiang *et al*, 2016). For example, stable isotope tracing and metabolic flux analyses identified a critical role
62 for the reductive carboxylation of glutamine-derived α-ketoglutarate for lipid biosynthesis in supporting tumor
63 growth (Metallo *et al*, 2011; Gameiro *et al*, 2013b; Scott *et al*, 2011; Wise *et al*, 2011), and metabolomic studies
64 identified aspartate as a limiting metabolite for cancer cell proliferation under hypoxia (Garcia-Bermudez *et al*,
65 2018). By contrast, comparatively little is known about metabolic adaptations of primary cells to hypoxia.
66 Indeed, the importance of reductive carboxylation or aspartate biosynthesis remains to be elucidated in these
67 cells. A more complete understanding of primary cell metabolic adaptations to hypoxia would provide an
68 important context for understanding how metabolic reprogramming supports normal cellular responses to
69 hypoxia, how these responses may be (mal)adaptive in a variety of disease contexts, and how the hypoxia
70 metabolic program in primary cells differs from that observed in cancer cells.

71 To address these questions, we have developed models of bioenergetic carbon flux in human lung fibroblasts
72 (LFs) and pulmonary artery smooth muscle cells (PASMCs) cultured in 21% or 0.5% oxygen. These cells may be
73 exposed to a wide range of oxygen concentrations *in vivo*, continue to proliferate despite hypoxic culture
74 conditions *in vitro*, and play important roles in the pathology of non-cancerous diseases in which tissue hypoxia
75 is a prominent feature, including pulmonary hypertension and pulmonary fibrosis. We found that hypoxia fails to
76 increase glycolysis in these primary cells despite robust up-regulation of the HIF-1α transcriptional program. In
77 normoxia, HIF-1α stabilization by the PHD inhibitor molidustat (BAY-85-3934, "BAY") (Flamme *et al*, 2014) did
78 increase glycolysis and lactate efflux; however, hypoxia blocked this response. These findings suggested that
79 important hypoxia-dependent regulatory mechanisms override the metabolic consequences of HIF-1α-
80 dependent glycolytic gene expression. Transcriptomic profiling identified a critical role for the transcription
81 factor MYC in the adaptive response to hypoxia. Using knockdown and overexpression approaches, we
82 demonstrated that MYC attenuates HIF-driven glycolysis in hypoxia and following HIF stabilization in normoxia.

83

RESULTS

Hypoxia uncouples HIF-dependent glycolytic gene expression from glycolytic metabolic flux

The goal of this study was to characterize hypoxia-induced metabolic changes in proliferating primary LFs and PASMCs. To accomplish this goal, we adopted a metabolic flux analysis technique that enabled us to link intracellular metabolic fluxes to cell proliferation rates. Metabolic flux analysis fits cell proliferation rate, extracellular flux measurements, and ^{13}C intracellular isotope labeling patterns to a computational model of cell metabolism (Antoniewicz, 2018). This analysis reconstructs comprehensive flux maps that depict the flow of carbon from extracellular substrates, through intracellular metabolic pathways, and into cell biomass and metabolic by-products (Young, 2014). These models assume that cells are at a metabolic pseudo-steady state over the experimental time course (Buescher *et al*, 2015). Exponential growth phase is thought to reflect metabolic pseudo-steady state as cells in culture steadily divide at their maximal condition-specific rate, provided nutrient supply does not become limiting (Buescher *et al*, 2015; Ahn & Antoniewicz, 2011). Thus, we first set out to define experimental conditions to capture exponential growth phase in normoxic and hypoxic cultures.

Cells were seeded and placed into hypoxia for 24 h prior to sample collection to provide adequate time for activation of the hypoxia-dependent transcriptional program (**Fig 1A**). We selected 0.5% oxygen for hypoxia as this level yielded the most reproducible phenotypic differences compared to 21% oxygen culture while being physiologically relevant and above the K_M of cytochrome *c* oxidase (electron transport chain complex IV) for oxygen (Lee *et al*, 2020; Wenger *et al*, 2015). From this starting point, we identified the optimal cell seeding density and time course to capture exponential cell growth (**Fig 1B**). LFs cultured in 0.5% oxygen grew more slowly than LFs cultured in 21% oxygen (**Fig 1C**), but slower growth was not associated with decreased cell viability (**Fig S1A**). As anticipated, hypoxic cells demonstrated robust stabilization of HIF-1α protein associated with up-regulation of downstream targets, such as glucose transporter 1 (GLUT1) and lactate dehydrogenase A (LDHA) (**Figs 1D-H**). These changes persisted for the duration of the experimental time course.

Having identified experimental conditions for exponential growth, we next determined the extracellular fluxes of glucose (GLC), lactate (LAC), pyruvate (PYR), and amino acids (**Figs 1I-J**). Flux calculations incorporated changes in cell number, extracellular metabolite concentrations, metabolite degradation rates, and medium evaporation over time (Murphy & Young, 2013) (**Figure S1**). Interestingly, while we observed a modest increase in glucose uptake, we found that hypoxia actually decreased lactate efflux (**Figs 1I**). This decrease in lactate efflux occurred despite activation of the HIF-1α transcriptional program as reflected by increased expression of

114 GLUT1 and LDHA. To test if more severe hypoxia would augment glycolysis, we cultured cells in 0.2% ambient
115 oxygen (**Fig S2**). Under these conditions, we observed no change in glucose or lactate fluxes, similar to 0.5%
116 oxygen culture. To test if this unexpected response was unique to LFs, we next studied PASMCs under 0.5%
117 oxygen conditions (**Fig S3**). PASMCs grew faster than LFs, and so samples were collected every 12 h for 48 h for
118 these cells. Again, similar to LFs at 0.5% and 0.2% oxygen, we observed no change in glucose uptake and
119 reduced lactate efflux in PASMCs regardless of HIF-1α stabilization. Together, these data suggest that hypoxia
120 uncouples HIF target gene expression and glycolytic flux in proliferating primary cells.

121 Given that hypoxia exposure did not increase glycolysis in LFs, we next wanted to determine how these cells
122 responded to HIF-1α stabilization in normoxia. To accomplish this, LFs were treated with the PHD inhibitor
123 molidustat (BAY, 10 μM) using a similar time course as our hypoxia experiments. Cells were treated with BAY for
124 24 h to activate the HIF transcriptional program prior to sample collection (**Fig 2A**). As with hypoxia, BAY
125 decreased cell growth rate (**Figs 2B-C**) and activated the HIF-1α transcriptional program (**Figs 2D-H**). Compared
126 to hypoxia, BAY treatment resulted in a similar activation of HIF-1α target gene transcription and protein
127 expression. Unlike hypoxia, however, HIF-1α stabilization in normoxia markedly increased glucose uptake and
128 lactate efflux (**Fig 2I**). This finding was consistent with the increased expression of glycolytic genes that we
129 observed. Interestingly, although hypoxia and BAY treatments resulted in similar increases in HIF-1α, GLUT1, and
130 LDHA, the glycolytic response was markedly different.

131 **Extracellular fluxes are treatment and cell-type dependent**

132 In addition to glucose and lactate, we also determined the extracellular fluxes of pyruvate and amino acids (**Figs**
133 **1J, 2J, S2J, S3J**). To our knowledge, this is the first comprehensive extracellular flux profiling of key metabolic
134 substrates in these primary cells. In LFs, overall, changes in these fluxes were modest, with hypoxia generally
135 decreasing the fluxes of all measured metabolites. These findings were similar with 0.2% oxygen exposure (**Fig**
136 **S2J**).

137 Notably, we observed a significant decrease in glutamine consumption in hypoxic LFs. This finding contrasts with
138 previous studies of cancer cell metabolism demonstrating increased glutamine uptake as a key feature of the
139 metabolic response to hypoxia (Metallo *et al*, 2011; Wise *et al*, 2011; Gameiro *et al*, 2013a). In these systems,
140 glutamine-derived α-ketoglutarate was reductively carboxylated by isocitrate dehydrogenase enzymes to
141 generate citrate for lipogenesis. In addition, glutamine has been shown to support TCA cycling in hypoxia in a
142 Burkitt lymphoma model (Le *et al*, 2012). Unlike LFs, PASMCs did exhibit a trend toward increased glutamine

143 uptake (**Figure S3J**), suggesting a greater reliance on these metabolic pathways in their adaptive response to
144 hypoxia.

145 In LFs, among all of the measured amino acid fluxes, proline consumption uniquely increased (**Fig 1J**). Hypoxia
146 increases collagen expression in these cells (Liu *et al*, 2013) and proline constitutes ~ 10% of the total amino acid
147 content of collagens. Together, these data suggest an important contribution of extracellular proline to collagen
148 production in hypoxic LFs as has been observed in other fibroblast cell lineages (Szoka *et al*, 2017).

149 In PASMCs, we observed increased consumption of the branched-chain amino acids (BCAAs) leucine and valine
150 as well as arginine (**Figure S3J**), which was not observed in LFs. BCAAs are transaminated by branch chain amino
151 transferase enzymes to branched chain α-keto acids (BCKAs). BCKAs are further metabolized to yield acyl-CoA
152 derivatives for lipogenesis or oxidation (Mann *et al*, 2021; Crown *et al*, 2015). Previous studies have shown that
153 hypoxia up-regulates arginase expression in hypoxic PASMCs (Chen *et al*, 2009; Xue *et al*, 2017) to support
154 polyamine and proline synthesis required for cell proliferation (Li *et al*, 2001). Interestingly, activation of these
155 metabolic pathways in hypoxia was not observed in LFs and suggests distinct metabolic vulnerabilities of these
156 different cell types.

157 Compared to hypoxia treatment, BAY demonstrated more modest effects on amino acid fluxes generally (**Figure**
158 **2J**). In particular, glutamate efflux was not affected by BAY treatment, while it was reduced by hypoxia. Alanine
159 efflux was increased by BAY treatment, but decreased by hypoxia. In addition to the glucose and lactate fluxes
160 noted above, these findings further highlight fundamental differences in the metabolic consequences of HIF
161 activation in normoxia and hypoxia.

162 **Isotope tracing reveals altered substrate utilization in hypoxia**

163 To investigate intracellular metabolic reprogramming in hypoxic cells, we performed ^{13}C stable isotope tracing
164 with [U-$^{13}C_6$]-glucose, [1,2-$^{13}C_2$]-glucose, and [U-$^{13}C_5$]-glutamine. Isotopic enrichment of downstream metabolites
165 in glycolysis and the TCA cycle were determined by LC-MS (**Figs S3, S4**). Overall, relatively small changes in the
166 patterns of isotope incorporation were observed following hypoxia or BAY treatment. The most substantial
167 differences were observed in pyruvate (PYR), the terminal product of glycolysis, and citrate (CIT), a central
168 metabolic node in TCA and fatty acid metabolism (**Figs 3A-C**). Both hypoxia and BAY treatments decreased
169 incorporation of glucose-derived carbon into pyruvate (**Fig 3A**) (*i.e.,* the unlabeled, or M0, fraction was greater).
170 This suggests a greater contribution from an unlabeled carbon source, such as extracellular pyruvate, lactate, or
171 alanine, than from glucose to the intracellular pyruvate pool following PHD inhibition.

172 Total citrate labeling from [U-$^{13}C_6$]-glucose was unchanged across the treatment conditions (**Fig 3B**). As
173 expected, we observed decreased M2 and M4 citrate isotopes, consistent with decreased pyruvate
174 dehydrogenase activity in hypoxia. Interestingly, we observed increased M3 and M5 citrate isotopes. Pyruvate
175 carboxylase catalyzes the carboxylation of pyruvate to oxaloacetate after which all three pyruvate carbons are
176 incorporated into citrate by citrate synthase. Thus, this labeling pattern suggests a more prominent contribution
177 of pyruvate carboxylase to sustain TCA cycle anaplerosis despite pyruvate dehydrogenase inhibition following
178 HIF-1α activation. By contrast to glucose labeling, much less citrate was labeled by glutamine with hypoxia or
179 BAY with a more pronounced effect of BAY treatment (**Fig 3C**), suggesting a less important contribution of
180 glutamine to TCA anaplerosis under these conditions. In addition, the overall fraction of M5 citrate resulting
181 from reductive carboxylation of glutamine-derived α-ketoglutarate was low (< 7%) (**Fig 3D**). Although a hypoxia-
182 mediated increase in M5 citrate was observed, the overall fraction was much less than the 10-20% levels
183 previously reported in cancer cells (Wise *et al*, 2011; Metallo *et al*, 2011).

184 The stable isotope labeling patterns in PASMCs were generally similar to LFs (**Figure S5**). The most notable
185 differences between LF and PASMC labeling were observed in citrate. Compared with LFs, a much lower fraction
186 of total citrate was labeled by glucose in PASMCs. Less activity of pyruvate carboxylase in these cells was
187 suggested by decreased M3 and M5 citrate isotopes after glucose labeling. Interestingly, the M5 citrate fraction
188 in PASMCs was more consistent with previous reports from the cancer literature (**Fig 3D**), suggesting a more
189 important role for glutamine metabolism for biomass synthesis in these cells.

190 **Glycolytic flux in hypoxia is closely coupled to cell growth rate**

191 The mass isotopomer distribution for a given metabolite is determined by the complex relationship among the
192 rate of isotope incorporation into the metabolic network, the contributions of unlabeled substrates, and fluxes
193 through related pathways. To clarify how these labeling patterns reflect changes in intracellular metabolite
194 fluxes, we next generated metabolic flux models incorporating the extracellular flux measurements and stable
195 isotope tracing data described above. Preliminary labeling time courses indicated that, even after 72 h of
196 labeling, intracellular metabolites did not reach isotopic steady state (**Fig S6**). Thus, we performed isotopically
197 non-stationary metabolic flux analysis as implemented by Isotopomer Network Compartment Analysis (INCA)
198 (Murphy & Young, 2013; Young *et al*, 2014; Jazmin & Young, 2013) (**Figs 3E-F, S7, Tables S1-S3**).

199 Overall, LF and PASMC metabolic fluxes were dominated by high rates of glucose uptake and glycolysis (**Figs**
200 **S7A-B**). Approximately 10% of cytoplasmic pyruvate enters the TCA cycle with the balance converted to lactate.
201 Consistent with extracellular flux measurements and isotope labeling patterns described above, significant

202 reductions in glycolysis, the TCA cycle, and amino acid metabolism were observed in the metabolic flux models
203 of LFs cultured in hypoxia (**Fig 3E**). A significant increase in pentose phosphate pathway flux was also observed,
204 although the absolute flux through this pathway is low. By contrast, HIF-1α activation by BAY in 21% oxygen
205 increased glycolysis and lactate fermentation by nearly 50% (**Figure 3F**), but had a similar effect on decreasing
206 serine and glutamine uptake as hypoxia. Metabolite fluxes in DMSO-treated cells were similar to 21% oxygen
207 controls (**Table S1-S2**).

208 In normoxia, the magnitude of intracellular metabolite fluxes was generally similar in LFs and PASMCs (**Figs S7A-**
209 **C, Tables S1, S3**). Compared to LFs, PASMCs had slower rates of glycolysis and faster rates of TCA metabolism
210 driven, in part, by increased glutamine uptake. In hypoxia, PASMCs exhibited similar decreases in glycolytic flux
211 as LFs but also a marked, and unexpected, increase in TCA flux (**Figure S7D**). The increased TCA flux in PASMCs
212 was driven by increased glutamine consumption. This finding is similar to a prior report of glutamine-driven
213 oxidative phosphorylation in hypoxic cancer cells (Fan *et al*, 2013), where oxidative phosphorylation continued
214 to provide the majority of cellular ATP even at 1% oxygen.

215 Given the global decrease in bioenergetic metabolic flux in hypoxic LFs, we hypothesized that these differences
216 may be a consequence of decreased growth rate. After normalizing metabolite fluxes in normoxia and hypoxia
217 to the cell growth rate, a modest increase (~10%) in glycolytic flux was observed (**Fig S7E**). This finding suggests
218 that, while glycolysis increases relative to growth rate in hypoxic cells, regulators of cell proliferation rate
219 override the consequences of the HIF-1α transcriptional program. Indeed, even after adjusting for cell growth
220 rate, the relative increase in glycolytic flux is modest compared to the marked up-regulation of glycolytic protein
221 levels and the glycolytic potential of these cells demonstrated by BAY treatment in normoxia. BAY treatment
222 decreased cell proliferation rate (**Fig 2B**), indicating that, unlike hypoxia, BAY treatment in normoxia uncouples
223 cell proliferation and metabolic flux.

224 **Hypoxia and BAY treatment increase lactate oxidation**

225 Although the metabolite exchange fluxes for bidirectional reactions tend to be poorly resolved by metabolic flux
226 analysis (Wiechert, 2007), two observations are worth highlighting (**Tables S1-S3**). First, consistent with the
227 stable isotope tracing results, the modeled rate of reductive carboxylation through reverse flux by isocitrate
228 dehydrogenase in LFs is low (~4 fmol/cell/h), unchanged by hypoxia, and modestly increased by BAY treatment.
229 By contrast, the rate of reductive carboxylation increases 6-fold in PASMCs in hypoxia, highlighting an important
230 role for this pathway in the metabolic response of PASMCs to decreased oxygen availability (**Fig 4A**).

231 Second, PHD inhibition is associated with a marked increase in the lactate transport exchange flux in LFs from ~
232 0 to 1,500 and 700 fmol/cell/h in 0.5% oxygen and BAY treatment conditions, respectively, with similar results in
233 PASMCs (**Fig 4B**). Since the net lactate transport flux is secretion, this observation suggests increased lactate
234 uptake with hypoxia or BAY treatment, a finding that may be consistent with the HIF-driven increased
235 expression of the reversible lactate transporter MCT4 (Contreras-Baeza *et al*, 2019). To investigate this
236 hypothesis, LFs and PASMCs were treated with [U-$^{13}C_3$] lactate (2 mM) and ^{13}C incorporation into intracellular
237 metabolites was analyzed by LC-MS (**Figs 4, S4, S5**). Lactate labeled ~50% of citrate and ~20% of downstream
238 TCA cycle metabolites in both LFs and PASMCs, indicating that lactate may be an important respiratory fuel
239 source in these cells even though lactate efflux is high. Although lactate has been used less commonly than
240 glucose and glutamine in stable isotope tracing studies, Faubert and colleagues (2017) demonstrated lactate
241 incorporation in human lung adenocarcinoma *in vivo*. In this study, lactate incorporation corresponded to
242 regions of high glucose uptake as determined by [^{18}F]-fluorodeoxyglucose positron emission tomography,
243 suggesting that lactate consumption can occur even in areas of high glucose utilization. Subsequently,
244 investigators have demonstrated the importance of lactate as a metabolic fuel *in vivo* (Hui *et al*, 2017; Hui *et al*,
245 2020). As predicated from our metabolic flux analysis, with hypoxia or BAY treatment, we observed increased
246 labeling of the TCA metabolites citrate (CIT), α-ketoglutarate (AKG), malate (MAL), and aspartate (ASP) in LFs.
247 Interestingly, although increased labeling of pyruvate was observed in hypoxic PASMCs, the label was not
248 incorporated into the TCA cycle as observed in LFs (**Fig S5**).

249 In addition to downstream metabolites, we also observed hypoxia- and BAY-dependent increases in lactate
250 incorporation in fructose bisphosphate (FBP) and 3-phosphoglycerate (3PG). This observation is consistent with
251 prior reports describing hypoxia-mediated increases in gluconeogenesis and glycogen synthesis (Owczarek *et al*,
252 2020; Pelletier *et al*, 2012; Favaro *et al*, 2012). These data suggest that lactate also makes a small (~5% carbon)
253 contribution to glycogen precursors. Together, these findings from stable isotope tracing of lactate reveal its
254 important contribution to primary cell metabolism under standard culture conditions, but also reveal increased
255 utilization of this substrate in hypoxia.

256 **Hypoxia abrogates the effects of BAY on increasing glycolysis**

257 To reconcile the differential effects of prolyl hydroxylase inhibition by hypoxia and BAY, we next addressed
258 whether hypoxia could suppress the effects of BAY on glucose and lactate fluxes (**Figs 5A-C**). LFs cultured in
259 standard growth medium were treated with BAY and placed in either 21% or 0.5% oxygen. Similar to previous
260 experiments, BAY treatment decreased cell growth rate, increased glucose uptake, and increased lactate efflux

261 in 21% oxygen. However, when combined with 0.5% oxygen, BAY treatment was unable to enhance lactate
262 efflux. These data clearly demonstrate that hypoxia antagonizes the effects of HIF-1α activation on glycolytic flux
263 in these cells.

264 To investigate these metabolic differences further, we performed metabolomic profiling of LFs treated for 72 h
265 with hypoxia or BAY separately or in combination. Both 0.5% oxygen and BAY treatment induced marked
266 changes in intracellular metabolite levels (**Fig S8**). Of 133 total metabolites, 99 were differentially regulated by
267 hypoxia and 54 were differentially regulated by BAY. Of the differentially regulated metabolites, 44 were
268 affected by both 0.5% oxygen and BAY treatment. Metabolite set enrichment analysis of KEGG biochemical
269 pathways identified increased enrichment of arginine and proline metabolism and fatty acid biosynthesis
270 pathways with hypoxia (**Fig S8D**). By contrast, BAY treatment was enriched for metabolites involved in
271 pentose/glucuronate interconversions and glycolysis (**Fig S8E**). Aspartate was the most significantly decreased
272 metabolite with both treatments, consistent with prior reports demonstrating an important role for HIF-1
273 regulation of aspartate biosynthesis in cancer cells (Garcia-Bermudez *et al*, 2018; Melendez-Rodriguez *et al*,
274 2019).

275 Principal component analysis revealed greater similarity among both treatment groups cultured in 0.5% oxygen
276 than among the BAY-treatment groups (**Fig 5D**). Moreover, these hypoxia-treated cells were well-segregated
277 from cells treated with BAY alone. These observations are, again, consistent with the results of the metabolic
278 flux models demonstrating an overriding effect of hypoxia *per se* on cell metabolism and highlighting important
279 differences between hypoxic and pharmacologic PHD inhibition. To identify the metabolic changes that depend
280 on hypoxia rather than BAY inhibition, we identified differentially regulated metabolites in BAY treated cells
281 cultured in normoxia and hypoxia (**Fig 5E**). Of 133 metabolites, 83 were significantly differentially regulated by
282 hypoxia in BAY-treated cells. An enrichment analysis of these differentially regulated metabolites demonstrated
283 up-regulation of arginine and proline metabolism and down-regulation of the TCA cycle as the most impacted by
284 hypoxia in BAY treated cells (**Fig 5F**). Indeed, leading edge analysis highlights negative enrichment scores
285 associated with all of the TCA metabolites detected by our platform (**Fig 5G**). This result indicates better
286 preservation of TCA cycle flux in normoxic BAY-treated cells than in hypoxic cells, as suggested by our metabolic
287 flux models where hypoxia resulted in a 1.5-2-fold reduction of TCA flux compared to a 1.1-1.5-fold reduction
288 with BAY treatment (**Fig 3**).

289 In addition to these differential effects on polar metabolite levels, we reasoned that another critical difference
290 between hypoxia and BAY treatment is the impact of hypoxia on cellular redox state. As oxygen deprivation

291 causes reductive stress (Xiao & Loscalzo, 2020), we next measured the impact of these treatments on
292 intracellular NAD(H) (**Figs 5H-J**). As expected, hypoxia increased the NADH/NAD^+ ratio, driven primarily by a
293 decrease in intracellular NAD^+. Interestingly, while BAY treatment increased the levels of NADH, a concomitant
294 increase in NAD^+ resulted in preservation of the NADH/NAD^+ ratio. As NADH accumulation is a putative inhibitor
295 of glycolytic flux (Tilton *et al*, 1991), this may be one mechanism by which glycolytic flux is decreased in hypoxia
296 but not following BAY treatment.

297 **Transcriptomic analysis identifies regulators of metabolism in hypoxia**

298 To identify the upstream regulators of the observed metabolic changes, we next performed RNA-seq
299 transcriptomic analysis of LFs treated with hypoxia or BAY, separately or together (**Fig 6, S9**). As anticipated,
300 both hypoxia and BAY treatment induced substantial changes in gene expression (**Fig S9A, S9B**). Of the 9,923
301 differentially expressed genes across both conditions, 869 (9%) were unique to BAY treatment in normoxia,
302 4,002 (40%) were shared by BAY and hypoxia, while 5,052 (51%) were unique to 0.5% hypoxia culture (**Fig S9C**).
303 This distribution of transcriptional changes was nearly identical to that observed for the metabolite changes (**Fig**
304 **S8C**), where half of the hypoxia-mediated changes overlapped with BAY treatment and half were unique to
305 hypoxia. Gene set enrichment analysis of these differentially regulated metabolites was performed using
306 Molecular Signatures Database "Hallmark" gene sets (Liberzon *et al*, 2015) (**Figs S9D-F**). As expected, both
307 treatments were associated with enrichment of the "hypoxia" and "glycolysis" gene sets.

308 Given the disparate effects of hypoxic and pharmacologic PHD inhibition on cellular metabolism described
309 above, we focused our transcriptomics analyses on the differences between hypoxia and BAY treatments.
310 Principal component analysis again demonstrated clear separation among the four treatment groups (**Fig 6A**).
311 The first and second principal components correspond to 0.5% oxygen and BAY treatments, respectively.
312 Consistent with our prior observations, the combination of 0.5% oxygen plus BAY was more similar to 0.5%
313 oxygen alone with decreased distance between both hypoxia-treated groups along the axis of the second
314 principal component, again, consistent with the hypothesis that hypoxia overrides the effects of BAY treatment.
315 To identify the transcripts driving these differences, we identified genes differentially expressed following
316 hypoxia in BAY-treated cells (**Fig 6B**). Interestingly, an enrichment analysis of these differentially expressed
317 transcripts identified pro-proliferative gene sets like "E2F targets", "G2/M checkpoint", and "MYC targets"
318 associated with hypoxia (**Fig 6C-E**). These findings were further supported by a transcription factor enrichment
319 analysis identifying enrichment of MYC transcription factor activity associated with hypoxia, but not BAY
320 treatment (**Fig 6F**). Classically, hypoxia and HIF activation are thought to inhibit cell proliferation by inhibiting

321 pro-proliferative MYC signaling (Koshiji *et al*, 2004). These results indicate that hypoxia-induced MYC activation
322 may be sustaining proliferation in these LFs. We reasoned that these pro-proliferative signals may also account
323 for the unexpected effects of hypoxia on glycolysis that we observed.

324 **MYC antagonizes HIF-dependent glycolytic fluxes**

325 To test the role of hypoxia-induced MYC activation in the metabolic response to hypoxia in proliferating primary
326 cells, we first measured MYC protein levels by immunoblot. Consistent with our bioinformatic results, we
327 observed increased MYC protein levels in hypoxia-treated cells, but not with BAY-treatment alone, where MYC
328 was decreased (**Fig 7A-B**). Together, these data suggest a model whereby hypoxia activates MYC and inhibits
329 HIF-driven increases in glycolysis. Inhibiting MYC in hypoxia, therefore, should increase glycolysis. Conversely,
330 HIF-dependent glycolysis after BAY treatment in normoxia should be sensitive to inhibition by MYC
331 overexpression (**Fig 7C**). To test the hypothesis that hypoxia-induced MYC expression inhibits glycolysis in
332 primary cells, we first combined MYC knockdown with hypoxia treatment (**Fig 7D-F**). As expected, MYC-deficient
333 cells proliferated more slowly in normoxia and MYC was essential for sustaining cell proliferation in hypoxia (**Fig
334 7E**). Consistent with our hypothesis, MYC-knockdown cells demonstrated increased lactate efflux with hypoxia
335 culture, unlike control siRNA-treated cells (**Fig 7F**). We next performed the complementary experiment to
336 determine whether MYC overexpression could attenuate the increase in glycolysis observed with BAY treatment
337 (**Fig 7G-I**). MYC increased the proliferation rate of DMSO-treated cells, although it did not augment the
338 proliferation rate of BAY-treated cells (**Fig 7H**). As expected, MYC overexpression blocked the BAY-stimulated
339 increase in lactate efflux. Together, these data suggest that hypoxia-induced MYC expression may be one factor
340 that uncouples the HIF transcriptional program from glycolytic flux in proliferating primary cells.

341

342 **DISCUSSION**

343 In this work, we used ^{13}C metabolic flux analysis to identify hypoxia-mediated metabolic changes in proliferating
344 human primary cells. Our principal finding was that hypoxia reduced, rather than increased, carbon flux through
345 glycolysis and lactate fermentation pathways despite robust activation of the HIF transcriptional program and
346 up-regulation of glycolytic genes. Certainly, the LFs studied here are capable of augmenting glycolysis in
347 response to HIF stabilization, as demonstrated by experiments with the PHD inhibitor BAY; however, these
348 effects are completely attenuated when BAY-treated cells are cultured in hypoxia. Together, these findings
349 suggest that changes in enzyme levels alone are insufficient to alter metabolic flux in hypoxia and point to the
350 importance of regulatory mechanisms that supersede the effects of HIF-dependent gene transcription in primary
351 cells.

352 Our data indicate that hypoxia-induced MYC expression is one such regulatory mechanism. MYC is a
353 transcription factor that regulates the expression of numerous genes involved in many biological processes,
354 including metabolism, proliferation, apoptosis, and differentiation (Dang *et al*, 2006; Li *et al*, 2020; Stine *et al*,
355 2015). As deregulated MYC activity has been associated with the majority of human cancers (Vita & Henriksson,
356 2006), much of our understanding of MYC regulation comes from studies using cancer cell models (Li *et al*, 2020;
357 Stine *et al*, 2015; Dang, 2012; Madden *et al*, 2021), while the role of MYC in the biology of untransformed cells is
358 less well understood. The literature describes a complex and reciprocal relationship between HIF and MYC that
359 depends on both environmental (*e.g.*, hypoxia) and cellular context (Li *et al*, 2020). Generally, HIF-1 has been
360 observed to inhibit MYC through multiple mechanisms (Koshiji *et al*, 2004, 2005; Gordan *et al*, 2007; Zhang *et al*,
361 2007), and this previous work is consistent with our present observations that HIF stabilization following BAY
362 treatment in normoxia decreased MYC protein and target gene expression. Conversely, MYC has been
363 implicated in increased HIF activity through transcriptional and post-transcriptional mechanisms (Zhang *et al*,
364 2009; Chen *et al*, 2013; Doe *et al*, 2012), primary in the context of malignant transformation. The observation
365 that MYC may antagonize the transcriptional effects of HIF to sustain primarily cell proliferation and metabolism
366 in hypoxia suggests a substantially different regulatory relationship than has been previously described.

367 Understanding how MYC transcriptional activity affects hypoxic primary cell metabolism is imperative to our
368 understanding of cellular adaptation to hypoxia. MYC stimulates the expression of nuclear-encoded
369 mitochondrial genes and promotes mitochondrial biogenesis, both directly and through activation of
370 mitochondrial transcriptional factor A (TFAM) (Li *et al*, 2005). Indeed, we found that the oxidative
371 phosphorylation gene set was relatively enriched with hypoxia culture of BAY-treated cells (**Fig 6C**). In this way,

372 hypoxic MYC activation may sustain energy production by oxidative phosphorylation, thereby decreasing the
373 energetic demands that would otherwise drive increased glycolytic flux. Beyond oxidative phosphorylation, MYC
374 regulates genes involved in many other intermediary metabolic pathways, including amino acids, nucleotides,
375 and lipids (Stine *et al*, 2015), that may also impact the central pathways of carbon metabolism studied in this
376 work.

377 Beyond MYC, the identification of other HIF-independent mechanisms regulating primary cell adaption to
378 hypoxia is of critical importance. Cells express several oxygen-dependent enzymes in addition to PHD whose
379 activities may be altered in hypoxia but not by PHD inhibition. For example, PHD is one of many α-ketoglutarate-
380 dependent dioxygenase enzymes that rely on molecular oxygen for their catalytic activity (Islam *et al*, 2018).
381 Jumonji-C (JmjC) domain-containing histone demethylases are other prominent members of this family whose
382 inhibition by hypoxia has been shown to cause rapid and HIF-independent induction of histone methylation
383 (Batie *et al*, 2019). Similarly, a recently described cysteamine dioxygenase has been shown to mediate the
384 oxygen-dependent degradation of Regulators of G protein Signaling 4 and 5 and IL-32 (Masson *et al*, 2019). In
385 addition to dioxygenase enzymes, electron transport chain dysfunction resulting from impaired Complex IV
386 activity leads to increased ROS production in hypoxia (Chandel *et al*, 1998). Mitochondrial ROS increase the half-
387 lives of several mRNAs in hypoxia, including MYC, independent of HIF stabilization (Guzy *et al*, 2005). Finally,
388 hypoxia imposes a reductive stress on cells associated with an increase in the $NADH/NAD^+$ ratio secondary to
389 impaired electron transport (**Fig 5K**)(Chance & Williams, 1955; Garofalo *et al*, 1988). NADH accumulation may
390 slow glycolysis *via* feedback inhibition of GAPDH (Tilton *et al*, 1991). Any or all of these molecular mechanisms
391 may also contribute to uncoupling glycolytic enzyme expression from glycolytic flux as observed in the
392 experiments described here.

393 In addition to its effects on cellular metabolism, another canonical role of HIF-1 activation is slowing of cellular
394 proliferation rate in the face of limited oxygen availability (Hubbi & Semenza, 2015), which we found here (**Figs**
395 **1B, 2B, 5A**). The effects of HIF-1 on cell proliferation rate are mediated, in part, by increased expression of
396 cyclin-dependent kinase inhibitor p21 (*CDKN1A*), inhibition of E2F targets (Gardner *et al*, 2001), and inhibition of
397 pro-proliferative MYC signaling (Koshiji *et al*, 2004). These transcriptional effects are precisely what we observed
398 in BAY treated LFs in normoxia. By contrast, hypoxia culture was associated with decreased expression of p21,
399 consistent with a previous report (Mizuno *et al*, 2009), as well as increased expression of MYC protein and
400 enrichment of MYC target genes. Indeed, the most marked differences between hypoxia and BAY treatment on
401 LF gene transcription were the up-regulation of pro-proliferative gene sets containing E2F targets and G2/M
402 checkpoint proteins. Much of this transcriptional response may be mediated by hypoxia-induced up-regulation

403 of MYC, which is known to stimulate cell cycle progression through its effects on the expression and activity of
404 cyclins, cyclin-dependent kinases, and cyclin-dependent kinase inhibitors (Hydbring *et al*, 2017). Clarifying the
405 complex interactions among HIFs, MYC, and cell proliferation will be important for understanding the cellular
406 response of these mesenchymal cells to tissue injury.

407 Taken together, these findings raise important questions regarding the cell-autonomous role of HIFs in the
408 hypoxia response. On an organismal level, HIFs drive expression of angiogenic and erythropoietic factors to
409 increase oxygen delivery to hypoxic tissues. Within individual cells, HIF-1α seems to be important for mitigating
410 the adverse effects of ROS formation by dysfunctional electron transport in the mitochondria. Indeed, hypoxia
411 increased oxygen consumption and ROS production in HIF-1α-null mouse embryonic fibroblasts (MEFs), which
412 was associated with increased cell death (Zhang *et al*, 2008). Interestingly, these cells also had increased ATP
413 levels compared to wild type, suggesting that mitochondrial function was adequate under 1% oxygen culture
414 conditions to support oxidative phosphorylation and to meet the energy needs of the cells. Given the
415 prominence of HIFs in mediating the transcriptional response to hypoxia, it is somewhat surprising that neither
416 PHD, HIFs, nor their downstream targets were found to be selectively essential as a function of oxygen tension
417 in a genome-wide CRISPR growth screen of K562 human lymphoblasts cultured in normoxia or hypoxia (Jain *et*
418 *al*, 2020). Similarly, knockout of HIF signaling did not affect growth, internal metabolite concentrations, glucose
419 consumption, or lactate production under hypoxia by human acute myeloid leukemia cells (Wierenga *et al*,
420 2019). Together with our results, these studies highlight the need for additional research linking hypoxia-
421 induced metabolic changes to their transcriptional and post-transcriptional regulatory mechanisms, particularly
422 in primary cells.

423 This work also highlights two specific metabolic features that appear to be important in the metabolic response
424 of primary cells to hypoxia. First, both LFs and PASMCs demonstrated notable incorporation of lactate-derived
425 carbon into intracellular metabolic pathways that increased with hypoxia and BAY treatments (**Figs 4, S4, S5**).
426 This finding is consistent with increasing evidence suggesting an important role for lactate as a metabolic fuel in
427 several organ systems (Faubert *et al*, 2013; Hui *et al*, 2017). Although typically considered a metabolic waste
428 product (Rabinowitz & Enerback, 2020), an important contribution of lactate *import* in supporting metabolic
429 homeostasis in the face of an ischemic insult, which is associated with increased extracellular lactate, is an
430 evolutionarily attractive hypothesis that merits further investigation. Second, PASMCs, but not LFs,
431 demonstrated significant rates of reductive carboxylation that increased in 0.5% oxygen (**Fig S5**). Reductive
432 carboxylation was first identified in hypoxic tumor cells where stable isotope tracing revealed ^{13}C incorporation
433 from labeled glutamine into lipids (Metallo *et al*, 2011; Gameiro *et al*, 2013a; Scott *et al*, 2011; Wise *et al*, 2011).

434 Hypoxia drives PASMC proliferation *in vivo* contributing to the development pulmonary hypertension in humans
435 and animal models. Isocitrate dehydrogenase has previously been implicated in the pathobiology of this disease
436 (Fessel *et al*, 2012), and our findings suggest that reductive carboxylation catalyzed by isocitrate dehydrogenase
437 may be a metabolic vulnerability of hypoxic PASMCs associated with pulmonary vascular disease.

438 Our finding that hypoxia was associated with decreased glycolysis and lactate fermentation was unexpected.
439 Several aspects of our experimental design may have contributed to this finding. First, our goal was to
440 understand how metabolic reprogramming may support cell proliferation in hypoxia. Thus, we measured
441 metabolite fluxes in cells during the exponential growth phase accounting for cell growth rate, metabolite
442 degradation rates, and medium evaporation with multiple measurements over a 72 h time course. Often, cells
443 are studied near confluence, where metabolic contributions to biomass production are less and the rate of
444 glycolysis in hypoxia may be higher. Second, we began our experimental treatments 24 h prior to collecting
445 samples to ensure that the hypoxia metabolic program was established prior to labeling. Similar studies (Metallo
446 *et al*, 2011; Grassian *et al*, 2014) typically placed cells into hypoxia at the time of labeling. Third, and perhaps
447 most importantly, these flux determinations were performed in human primary cell cultures rather than
448 immortalized cell lines. Although both cell types used in this study were derived from lung, we anticipate that
449 many of our findings will be generalizable to primary cells from different tissues.

450 In summary, in this metabolic flux analysis of proliferating human primary cells *in vitro*, we have demonstrated
451 that MYC uncouples an increase in HIF-dependent glycolytic gene transcription from glycolytic flux in hypoxia.
452 Indeed, the degree of metabolic reprogramming in hypoxia was modest and suggests close coupling between
453 proliferation and metabolism. In light of our findings, additional studies are warranted to clarify the role of HIFs
454 in mediating the metabolic response to hypoxia, to determine how MYC activity is regulated by hypoxia, and to
455 identify other key regulators of hypoxic metabolic reprogramming in primary cells. Moreover, these data
456 strongly caution investigators against drawing conclusions about metabolite flux from measures of gene
457 transcription alone.

458

459 **MATERIALS AND METHODS**

460 **Cell culture**

461 Primary normal human lung fibroblasts (LFs) were purchased from Lonza (CC-2512) and cultured in FGM-2
462 (Lonza CC-3132). Cells from two donors were used in these studies: #33652 (56 y.o., male) and #29132 (19 y.o.,
463 female). Primary human pulmonary artery smooth muscle cells were purchased from Lonza (CC-2581) and
464 cultured in SmGM-2 (Lonza CC-3182). Cells from three donors were used in these studies: #30020 (64 y.o.,
465 male), #27662 (35 y.o., male), #26698 (51 y.o., male), and #19828 (51 y.o., male). Cell authentication was
466 performed by the vendor. Cells were maintained in a standard tissue culture incubator in 5% CO_2 at 37 °C.

467 **Metabolic flux protocol**

468 For extracellular flux measurements, cells were seeded in either standard growth medium or MCDB131 medium
469 lacking glucose, glutamine, and phenol red (genDEPOT) which was supplemented with 2% dialyzed fetal bovine
470 serum (Mediatech) and naturally labeled glucose and glutamine ("light" labeling medium). For LFs, glucose was
471 supplemented at 8 mM and glutamine was supplemented at 1 mM. For PASMCs, glucose was supplemented at
472 5.55 mM and glutamine was supplemented at 10 mM. These concentrations match the concentrations of these
473 substrates determined in standard growth medium. Preliminary experiments were performed to identify the
474 optimal cell seeding density, exponential growth phase, and labeling duration consistent with metabolic and
475 isotopic steady state. On Day -1, 25,000 cells were seeded in a 35 mm dish in "light" labeling medium. Hypoxia-
476 treated cells were transferred to a tissue culture glovebox set at 0.5% oxygen and 5% CO_2 (Coy Lab Products).
477 Medium was supplemented with DMSO 0.1% or BAY (10 µM) for these treatment conditions. On Day 0, cells
478 were washed with PBS and the medium was changed to either "light" labeling medium for flux measurements or
479 "heavy" labeling medium containing [1,2-$^{13}C_2$]-glucose, [U-$^{13}C_6$]-glucose, [U-$^{13}C_5$]-glutamine, or [U-$^{13}C_2$]-lactate
480 for tracer experiments. For LFs, samples were collected on Day 0 and every 24 h for 72 h. For PASMCs, samples
481 were collected on Day 0 and every 12 h for 48 h. Medium and cell lysates were collected at each time point for
482 intra- and extracellular metabolite measurements and total DNA quantification. Dishes without cells were
483 weighed daily to correct for evaporative medium losses and to empirically determine degradation and
484 accumulation rates of metabolites. Medium samples and cell lysates for DNA measurement were stored at -80
485 °C until analysis. Each individual experiment included triplicate wells for each treatment and time point, and
486 each experiment was repeated 4-8 times.

487 **Cell count**

488 Direct cell counts of trypsinized cell suspensions in PBS were obtained following staining with propidium iodide
489 and acridine orange using a LUNA-FL fluorescence cell counter (Logos Biosystems). Indirect cell counts for flux
490 measurements were interpolated from total DNA quantified using the Quant-iT PicoGreen dsDNA Assay Kit
491 (Thermo). Cells were washed once with two volumes of PBS, lysed with Tris-EDTA buffer containing 2% Triton X-
492 100, and collected by scraping. Total DNA in 10 µL of lysate was determined by adding 100 µL of 1X PicoGreen
493 dye in Tris-EDTA buffer and interpolating the fluorescence intensity with a standard curve generated using the λ
494 DNA standard. Cell counts were interpolated from a standard curve of DNA obtained from known cell numbers
495 seeded in basal medium (**Fig S1B-C**). No difference in total cellular DNA was identified between normoxia and
496 hypoxia cultures (**Fig S1D**).

497 **Immunoblots**

498 Cells were washed with one volume of PBS and collected by scraping in PBS. Cell suspensions were centrifuged
499 at 5,000 ×*g* for 5 min at 4 °C. Pellets were lysed in buffer containing Tris 10 mM, pH 7.4, NaCl 150 mM, EDTA 1
500 mM, EGTA 1 mM, Triton X-100 1% v/v, NP-40 0.5% v/v, and Halt Protease Inhibitor Cocktail (Thermo). Protein
501 concentrations were determined by BCA Protein Assay (Thermo). Lysates were normalized for protein
502 concentration and subjected to SDS-PAGE separation on stain-free tris-glycine gels (Bio-Rad), cross-linked and
503 imaged with the Chemidoc system (Bio-Rad), transferred to PVDF membranes with the Trans-Blot Turbo transfer
504 system (Bio-Rad), imaged, blocked in 5% blocking buffer (Bio-Rad), blotted in primary and secondary antibodies,
505 and developed using WesternBright ECL (Advansta). Band signal intensity was normalized to total protein per
506 lane as determined from the stain-free gel or membrane images.

507 **RT-qPCR**

508 Total RNA was isolated from cells with the RNeasy Mini Kit (Qiagen). cDNA was synthesized from 0.25-1.00 ng
509 RNA with the High Capacity cDNA Reverse Transcription Kit (Applied Biosystems). RT-qPCR analysis was
510 performed with an Applied Biosystems 7500 Fast Real Time PCR System with TaqMan Universal PCR Master Mix
511 and pre-designed TaqMan gene expression assays (Life Technologies). Relative expression levels were calculated
512 using the comparative cycle threshold method referenced to *ACTB*.

513 **Glucose assay**

514 Medium samples were diluted 10-fold in PBS. Glucose concentration was determined using the Glucose
515 Colorimetric Assay Kit (Cayman) according to the manufacturer's protocol. Standards were prepared in PBS.

516 **Lactate assay**

517 Medium samples were diluted 10-fold in PBS. Glucose concentration was determined using the L-Lactate Assay
518 Kit (Cayman). Medium samples did not require deproteinization, otherwise the samples were analyzed
519 according to the manufacturer's protocol. Standards were prepared in PBS.

520 **Pyruvate assay**

521 Pyruvate was measured using either an enzymatic assay (most samples) or an HPLC-based assay (medium from
522 0.2% oxygen experiments). For the enzymatic assay, medium samples were diluted 20-fold in PBS. Pyruvate
523 concentration was determined using the Pyruvate Assay Kit (Cayman). Medium samples did not require
524 deproteinization, otherwise the samples were analyzed according to the manufacturer's protocol. Standards
525 were prepared in PBS. For the HPLC assay, 2-oxovaleric acid was added to medium samples as an internal
526 standard. Samples were subsequently deproteinized with 2 volumes of ice-cold acetone. Supernatants were
527 evaporated to < 50% of the starting volume at 43 °C in a SpeedVac concentrator (Thermo Savant) and
528 reconstituted to the starting volume with HPLC-grade water prior to derivatization. Samples were derivatized
529 1:1 by volume with *o*-phenylenediamine (25 mM in 2 M HCl) for 30 min at 80 °C. Derivatized pyruvate was
530 separated with a Poroshell HPH C-18 column (2.1 × 100 mm, 2.7 µm) on an Infinity II high-performance liquid
531 chromatography system with fluorescence detection of OPD-derivatized α-keto acids as described previously
532 (Guarino *et al*, 2019).

533 **Amino acid assay**

534 Medium amino acid concentrations were determined following the addition of norvaline and sarcosine internal
535 standards and deproteinization with 2 volumes of ice-cold acetone. Supernatants were evaporated to < 50% of
536 the starting volume at 43 °C in a SpeedVac concentrator (Thermo Savant) and reconstituted to the starting
537 volume with HPLC-grade water prior to analysis. Amino acids in deproteinized medium were derivatized with *o*-
538 phthalaldehyde (OPA) and 9-fluorenylmethylchloroformate (FMOC) immediately prior to separation with a
539 Poroshell HPH-C18 column (4.6 × 100 mm, 2.7 µm) on an Infinity II high-performance liquid chromatography

540 system with ultraviolet and fluorescence detection of OPA- and FMOC-derivatized amino acids, respectively,
541 according to the manufacturer's protocol (Agilent) (Long, 2017).

542 **MYC knockdown**

543 Approximately 1.25 M LFs were reverse transfected in 6-cm dishes with 40 pmol siMYC or non-targeting siCTL
544 pools (Dharmacon) and 20 µL RNAiMAX (Thermo) in 500 µL OptiMEM (Thermo). After 24 h, cells were collected
545 by trypsinization and re-seeded as described in *Metabolic flux protocol* above for growth rate and lactate efflux
546 measurements.

547 **MYC overexpression**

548 LFs were seeded at 25,000 cells per 35 mm dish on Day -2. On Day -1, cells were transduced with adenovirus for
549 MYC (Vector Biolabs) or YFP overexpression (Oldham *et al*, 2015). After 24 h, the medium was changed and
550 samples were collected as described in *Metabolic flux protocol* above.

551 **Flux calculations**

552 The growth rate (μ) and flux (v) for each measured metabolite were defined as follows (Murphy & Young, 2013):

553
$$\frac{dX}{dt} = \mu X \qquad (1)$$
$$\frac{dM}{dt} = -kM + vX \qquad (2)$$

554 where X is the cell density, k is the first-order degradation or accumulation rate, and M is the mass of the
555 metabolite. These equations are solved as follows:

556
$$X = X_0 e^{\mu t} \qquad (3)$$
$$Me^{kt} = \frac{vX_0}{\mu + k}\left(e^{(\mu+k)t} - 1\right) + M_0 \qquad (4)$$

557 Growth rate (μ) and cell count at time 0 (X_0) were determined by robust linear modeling of the logarithm of cell
558 count as a function of time (t). Metabolite mass was calculated from the measured metabolite concentrations
559 and predicted well volume accounting for evaporative losses (**Fig S1E**). First-order degradation and accumulation
560 rates were obtained from robust linear modeling of metabolite mass *v*. time in unconditioned culture medium.
561 Rates that significantly differed from 0 by Student's *t*-test were incorporated into the flux calculations. Final

562 fluxes were obtained by robust linear modeling of Me^{kt} *versus* $\left(e^{(\mu+k)t}-1\right)$ to determine the slope from which
563 v was calculated using equation (4).

564 **Metabolomics**

565 ***Metabolite extraction***

566 Intracellular metabolites were obtained after washing cells with 2 volumes of ice-cold PBS and floating on liquid
567 nitrogen. Plates were stored at -80 °C until extraction. Metabolites were extracted with 1 mL 80% MeOH pre-
568 cooled to -80 °C containing 10 nmol [D_8]-valine as an internal standard (Cambridge Isotope Labs). Insoluble
569 material was removed by centrifugation at 21,000 ×*g* for 15 min at 4 °C. The supernatant was evaporated to
570 dryness at 42 °C using a SpeedVac concentrator (Thermo Savant). Samples were resuspended in 35 µL LC-MS-
571 grade water prior to analysis.

572 ***Acquisition parameters***

573 LC-MS analysis was performed on a Vanquish ultra-high-performance liquid chromatography system coupled to
574 a Q Exactive orbitrap mass spectrometer by a HESI-II electrospray ionization probe (Thermo). External mass
575 calibration was performed weekly. Metabolite samples (2.5 µL) were separated using a ZIC-pHILIC stationary
576 phase (2.1 × 150 mm, 5 µm) (Merck). The autosampler temperature was 4 °C and the column compartment was
577 maintained at 25 °C. Mobile phase A was 20 mM ammonium carbonate and 0.1% ammonium hydroxide. Mobile
578 phase B was acetonitrile. The flow rate was 0.1 mL/min. Solvent was introduced to the mass spectrometer *via*
579 electrospray ionization with the following source parameters: sheath gas 40, auxiliary gas 15, sweep gas 1, spray
580 voltage +3.0 kV for positive mode and -3.1 kV for negative mode, capillary temperature 275 °C, S-lens RF level
581 40, and probe temperature 350 °C. Data were acquired and peaks integrated using TraceFinder 4.1 (Thermo).

582 ***Stable isotope quantification***

583 All metabolites except fructose 2,6-bisphosphate (FBP) and 3-phosphoglycerate (3PG) were measured using the
584 following mobile phase gradient: 0 min, 80% B; 5 min, 80% B; 30 min, 20% B; 31 min, 80% B; 42 min, 80% B. The
585 mass spectrometer was operated in selected ion monitoring mode with an m/*z* window width of 9.0 centered
586 1.003355-times half the number of carbon atoms in the target metabolite. The resolution was set at 70,000 and
587 AGC target was 1×10^5 ions. Peak areas were corrected for quadrupole bias as in Kim *et al.* (2015). Mass isotope
588 distributions for FBP and 3PG were calculated from full scan chromatograms as described below. Raw mass

589 isotopomer distributions were corrected for natural isotope abundance using a custom R package (mzrtools,
590 https://github.com/oldhamlab/mzrtools) employing the method of Fernandez, *et al.* (1996).

591 ***Metabolomic profiling***

592 For metabolomic profiling and quantification of isotopic enrichment for FBP and 3PG, the following mobile
593 phase gradient was used: 0 min, 80% B; 20 min, 20% B; 20.5 min, 80% B; 28 min, 80% B; 42 min, 80% B. The
594 mass spectrometer was operated in polarity switching full scan mode from 70-1000 m/*z*. Resolution was set to
595 70,000 and the AGC target was 1×10^6 ions. Peak identifications were based on an in-house library of authentic
596 metabolite standards previously analyzed utilizing this method. For metabolomics studies, pooled quality control
597 (QC) samples were injected at the beginning, end, and between every four samples of the run. Raw peak areas
598 for each metabolite were corrected for instrument drift using a cubic spline model of QC peak areas. Low quality
599 features were removed on the basis of a relative standard deviation greater than 0.2 in the QC samples and a
600 dispersion ratio greater than 0.4 (Broadhurst *et al*, 2018). Missing values were imputed using random forest.
601 Samples peak areas were normalized using probabilistic quotient normalization (Dieterle *et al*, 2006).
602 Differentially regulated metabolites were identified using limma (Ritchie *et al*, 2015). Metabolite set enrichment
603 analysis was performed using the fgsea package (Korotkevich *et al*, 2021) with KEGG metabolite pathways
604 (Kanehisa & Goto, 2000).

605 **Biomass determination**

606 The dry weight of LFs was determined to be 493 pg/cell. The dry weight of PASMCs was determined to be 396
607 pg/cell. These values were estimated by washing 3×10^6 cells twice in PBS and thrice in ice-cold acetone prior to
608 drying overnight in a SpeedVac. The composition of the dry cell mass was estimated from the literature (Quek *et*
609 *al*, 2010; Sheikh *et al*, 2005), and stoichiometric coefficients were determined as described (Murphy *et al*, 2013;
610 Zamorano *et al*, 2010).

611 **Metabolic flux analysis**

612 Metabolic flux analysis was performed using the elementary metabolite unit-based software package INCA
613 (Young, 2014). Inputs to the model include the chemical reactions and atom transitions of central carbon
614 metabolism, extracellular fluxes, the identity and composition of ^{13}C-labeled tracers, and the MIDs of labeled
615 intracellular metabolites. The metabolic network was adapted from previously published networks (Murphy *et*
616 *al*, 2013; Vacanti *et al*, 2014) and comprises 48 reactions representing glycolysis, the pentose phosphate

617 pathway, the tricarboxylic acid cycle, anaplerotic pathways, serine metabolism, and biomass synthesis. The
618 network includes seven extracellular substrates (aspartate, cystine, glucose, glutamine, glycine, pyruvate, serine)
619 and five metabolic products (alanine, biomass, glutamate, lactate, lipid). Models were fit using three ^{13}C-labeled
620 tracers, [1,2-$^{13}C_2$] glucose, [U-$^{13}C_6$] glucose, and [U-$^{13}C_5$] glutamine. The MIDs of twelve metabolites (2-
621 oxoglutarate, 3-phosphoglycerate, alanine, aspartate, citrate, fructose bisphosphate, glutamate, glutamine,
622 lactate, malate, pyruvate, serine) were used to constrain intracellular fluxes. The following assumptions were
623 made:

624 1. Metabolism was at steady state.
625 2. Labeled CO_2 produced during decarboxylation reactions left the system and did not re-incorporate
626 during carboxylation reactions.
627 3. Protein turnover occurred at a negligible rate compared to glucose and glutamine consumption.
628 4. Acetyl-CoA and pyruvate existed in cytosolic and mitochondrial pools. Aspartate, fumarate,
629 oxaloacetate, and malate were allowed to exchange freely between the compartments.
630 5. The per cell biomass requirements of LFs and PASMCs were similar to published estimates from other
631 cell types (Quek *et al*, 2010; Sheikh *et al*, 2005).
632 6. Succinate and fumarate are symmetric molecules that have interchangeable orientations when
633 metabolized by TCA cycle enzymes.

634 Flux estimation was repeated a minimum of 50 times from random initial values. Results were subjected to a χ^2
635 statistical test to assess goodness-of-fit. Accurate 95% confidence intervals were computed for estimated
636 parameters by evaluating the sensitivity of the sum-of-square residuals to parameter variations (Antoniewicz *et*
637 *al*, 2006; Murphy *et al*, 2013).

638 **NAD(H) assay**

639 Cellular NAD^+ and NADH were measured using an enzymatic fluorometric cycling assay based on the reduction
640 of NAD^+ to NADH by alcohol dehydrogenase (ADH) and subsequent electron transfer to generate the fluorescent
641 molecule resorufin (Oldham *et al*, 2015). Briefly, cells were washed twice with one volume PBS. Pyridine
642 nucleotides were extracted on ice with buffer containing 50% by volume PBS and 50% lysis buffer (100 mM
643 sodium carbonate, 20 mM sodium bicarbonate, 10 mM nicotinamide, 0.05% by volume Triton-X-100, 1% by
644 mass dodecyltrimethylammonium bromide) and collected by scraping. Extracts were divided equally and 0.5
645 volume of 0.4 N HCl was added to one sample. Both extracts were heated at 65 °C for 15 min to degrade
646 selectively either the oxidized (buffer) or reduced (HCl) nucleotides. The reaction was cooled on ice and

647 quenched by adding 0.5 M Tris-OH to the acid-treated samples or 0.2 N HCl plus 0.25 M Tris-OH to the buffer
648 samples. Samples were then diluted in reaction buffer (50 mM EDTA and 10 mM Tris, pH 7.06). Cell debris was
649 pelleted by centrifugation, and 50 µL was incubated for 2 h with 100 µL reaction buffer containing 0.6 M EtOH,
650 0.5 mM phenazine methosulfate, 0.05 mM resazurin, and 0.1 mg/mL ADH. Fluorescence intensities were
651 measured with a Spectramax Gemini XPS (Molecular Devices) with excitation 540 nm, emission 588 nm, and 550
652 nm excitation cut-off filter. Sample intensities were compared to a standard curve generated from known
653 concentrations of NADH. The ratio of fluorescence in buffer-extracted to acid-extracted samples corresponds to
654 the $NADH/NAD^+$ ratio. Absolute NADH and NAD^+ were normalized to estimated cell counts from total DNA
655 quantification as described above.

656 **RNA-seq**

657 RNA was collected from LFs treated for three days ± hypoxia ± BAY as described above. Four biological replicates
658 were analyzed. Library construction and sequencing was performed by BGI Genomics using 100 bp paired end
659 analysis and a read depth of 50 M reads per sample. Sequences were deposited in the NIH SRA (PRJNA721596).
660 Sequences were mapped to the human GRCh38 primary assembly and counts summarized using Rsubread (Liao
661 *et al*, 2019). This data is available from the Oldham Lab GitHub repository
662 (https://github.com/oldhamlab/rnaseq.lf.hypoxia.molidustat). Differentially expressed transcripts were
663 identified using DESeq2 (Love *et al*, 2014). Gene set enrichment and transcription factor enrichment was
664 performed using the fgsea and DoRothEA R packages, respectively (Korotkevich *et al*, 2021; Garcia-Alonso *et al*,
665 2019).

666 **Quantification and Statistical Analysis**

667 The raw data and annotated analysis code necessary to reproduce this manuscript are contained in an R package
668 research compendium available from the Oldham Lab GitHub repository
669 (https://github.com/oldhamlab/Copeland.2022.hypoxia.flux). Data analysis, statistical comparisons, and
670 visualization were performed in R (R Core Team, 2022) using the packages referenced in the data supplement.
671 Experiments included technical and biological replicates as noted above. The number of biological replicates (n)
672 is indicated in the figure legends. Summary data show the mean ± SEM. Outliers were identified using twice the
673 median absolute deviation as a cutoff threshold. Comparisons were performed using linear mixed-effects
674 models with oxygen, treatment, and their interaction as fixed effects and biological replicate as a random effect.
675 Significant differences in estimated marginal means were identified by comparisons to the multivariate *t*

676 distribution. Metabolomics and RNA-seq data were analyzed as described above. Probability values less than
677 0.05 were considered statistically significant.

678

679 **Key Resources Table**

REAGENT or RESOURCE	SOURCE	IDENTIFIER
Antibodies		
HIF-1α	BD Biosciences	610958
c-MYC	Cell Signaling Technologies	D84C12
LDHA	Cell Signaling Technologies	2012
HRP-α-Rabbit IgG	Cell Signaling Technologies	7074
HRP-α-Mouse IgG	Cell Signaling Technologies	7076
Bacterial and virus strains		
c-MYC adenovirus	Vector Biolabs	1285
YFP adenovirus	Oldham et al., 2015	
Chemicals, peptides, and recombinant proteins		
[1,2-$^{13}C_2$]-glucose	Cambridge Isotope Labs	CLM-504-PK
[U-$^{13}C_6$]-glucose	Cambridge Isotope Labs	CLM-1396-PK
[U-$^{13}C_5$]-glutamine	Cambridge Isotope Labs	CLM-1822-H-PK
[U-$^{13}C_3$]-lactate	Sigma	485926
Molidustat (BAY-85-3934)	Cayman	15297
Critical commercial assays		
Glucose colorimetric assay kit	Cayman	10009582
L-Lactate assay kit	Cayman	700510
Pyruvate assay kit	Cayman	700470
Depositied data		
Raw and analyzed data	This paper	https://github.com/oldhamlab/Copeland.2022.hypoxia.flux
RNA-seq reads	This paper	SRA: PRJNA721596
Summarized RNA-seq data	This paper	https://github.com/oldhamlab/rnaseq.lf.hypoxia.molidustat
Experimental models: Cell lines		
Normal human lung fibroblasts	Lonza	CC-2512

REAGENT or RESOURCE	SOURCE	IDENTIFIER
Pulmonary artery smooth muscle cells	Lonza	CC-2581
Oligonucleotides		
ACTB (Hs03023943_g1)	Life Technologies	4351370
GLUT1 (Hs00892681_m1)	Life Technologies	4351370
LDHA (Hs00855332_g1)	Life Technologies	4351370
MYC ON-TARGETplus siRNA	Dharmacon	L-003282-02-0005
ON-TARGETplus non-targeting control pool	Dharmacon	D-001810-10-05

680

ACKNOWLEDGEMENTS

This work was supported by grants from the NIH (K08HL128802), American Lung Association, Pulmonary Hypertension Association, and the American Thoracic Society Foundation to W.M.O and from the NIH (U01HG007690, U54HL119145, R01HL155107, R01HL155096) and the American Heart Association (D700382, CV-19) to J.L.

AUTHOR CONTRIBUTIONS

W.M.O. conceived and designed the analysis. C.A.C., B.A.O., D.R.Z., S.M., K.L., and W.M.O. collected the data. J.D.Y. and W.M.O. contributed data or analysis tools. W.M.O. performed the analysis. W.M.O. drafted the manuscript. All authors participated in interpreting the results and revising the manuscript. All authors approve the final submission.

CONFLICT OF INTEREST

The authors declare that they have no conflicts of interest.

694 **REFERENCES**

695 Ahn WS & Antoniewicz MR (2011) Metabolic flux analysis of CHO cells at growth and non-growth phases using
696 isotopic tracers and mass spectrometry. *Metab Eng* 13: 598–609

697 Antoniewicz MR (2018) A guide to 13C metabolic flux analysis for the cancer biologist. *Exp Mol Med* 50: 1–13

698 Antoniewicz MR, Kelleher JK & Stephanopoulos G (2006) Determination of confidence intervals of metabolic
699 fluxes estimated from stable isotope measurements. *Metab Eng* 8: 324–37

700 Batie M, Frost J, Frost M, Wilson JW, Schofield P & Rocha S (2019) Hypoxia induces rapid changes to histone
701 methylation and reprograms chromatin. *Science* 363: 1222–1226

702 Broadhurst D, Goodacre R, Reinke SN, Kuligowski J, Wilson ID, Lewis MR & Dunn WB (2018) Guidelines and
703 considerations for the use of system suitability and quality control samples in mass spectrometry assays applied
704 in untargeted clinical metabolomic studies. *Metabolomics* 14: 72

705 Buescher JM, Antoniewicz MR, Boros LG, Burgess SC, Brunengraber H, Clish CB, DeBerardinis RJ, Feron O, Frezza
706 C, Ghesquiere B, *et al* (2015) A roadmap for interpreting (13)C metabolite labeling patterns from cells. *Curr Opin*
707 *Biotechnol* 34: 189–201

708 Chance B & Williams GR (1955) Respiratory enzymes in oxidative phosphorylation. III. The steady state. *J Biol*
709 *Chem* 217: 409–27

710 Chandel NS, Maltepe E, Goldwasser E, Mathieu CE, Simon MC & Schumacker PT (1998) Mitochondrial reactive
711 oxygen species trigger hypoxia-induced transcription. *Proc Natl Acad Sci U S A* 95: 11715–20

712 Chen B, Calvert AE, Cui H & Nelin LD (2009) Hypoxia promotes human pulmonary artery smooth muscle cell
713 proliferation through induction of arginase. *American Journal of Physiology-Lung Cellular and Molecular*
714 *Physiology* 297: L1151–L1159

715 Chen C, Cai S, Wang G, Cao X, Yang X, Luo X, Feng Y & Hu J (2013) c-Myc enhances colon cancer cell-mediated
716 angiogenesis through the regulation of HIF-1α. *Biochem Biophys Res Commun* 430: 505–511

717 Contreras-Baeza Y, Sandoval PY, Alarcon R, Galaz A, Cortes-Molina F, Alegria K, Baeza-Lehnert F, Arce-Molina R,
718 Guequen A, Flores CA, *et al* (2019) Monocarboxylate transporter 4 (MCT4) is a high affinity transporter capable
719 of exporting lactate in high-lactate microenvironments. *J Biol Chem* 294: 20135–20147

720 Crown SB, Marze N & Antoniewicz MR (2015) Catabolism of Branched Chain Amino Acids Contributes
721 Significantly to Synthesis of Odd-Chain and Even-Chain Fatty Acids in 3T3-L1 Adipocytes. *PLoS One* 10: e0145850

722 Dang CV (2012) MYC on the path to cancer. *Cell* 149: 22–35

723 Dang CV, O'Donnell KA, Zeller KI, Nguyen T, Osthus RC & Li F (2006) The c-Myc target gene network. *Semin*
724 *Cancer Biol* 16: 253–264

725 Dieterle F, Ross A, Schlotterbeck G & Senn H (2006) Probabilistic quotient normalization as robust method to
726 account for dilution of complex biological mixtures. Application in 1H NMR metabonomics. *Anal Chem* 78: 4281–
727 90

728 Doe MR, Ascano JM, Kaur M & Cole MD (2012) Myc posttranscriptionally induces HIF1 protein and target gene
729 expression in normal and cancer cells. *Cancer Res* 72: 949–957

730 Fan J, Kamphorst JJ, Mathew R, Chung MK, White E, Shlomi T & Rabinowitz JD (2013) Glutamine-driven oxidative
731 phosphorylation is a major ATP source in transformed mammalian cells in both normoxia and hypoxia. *Mol Syst*
732 *Biol* 9: 712

733 Faubert B, Boily G, Izreig S, Griss T, Samborska B, Dong Z, Dupuy F, Chambers C, Fuerth BJ, Viollet B, *et al* (2013)
734 AMPK is a negative regulator of the Warburg effect and suppresses tumor growth in vivo. *Cell Metab* 17: 113–24

735 Faubert B, Li KY, Cai L, Hensley CT, Kim J, Zacharias LG, Yang C, Do QN, Doucette S, Burguete D, *et al* (2017)
736 Lactate Metabolism in Human Lung Tumors. *Cell* 171: 358–371 e9

737 Favaro E, Bensaad K, Chong MG, Tennant DA, Ferguson DJ, Snell C, Steers G, Turley H, Li JL, Gunther UL, *et al*
738 (2012) Glucose utilization via glycogen phosphorylase sustains proliferation and prevents premature senescence
739 in cancer cells. *Cell Metab* 16: 751–64

740 Fernandez CA, Des Rosiers C, Previs SF, David F & Brunengraber H (1996) Correction of 13C mass isotopomer
741 distributions for natural stable isotope abundance. *J Mass Spectrom* 31: 255–62

742 Fessel JP, Hamid R, Wittmann BM, Robinson LJ, Blackwell T, Tada Y, Tanabe N, Tatsumi K, Hemnes AR & West JD
743 (2012) Metabolomic analysis of bone morphogenetic protein receptor type 2 mutations in human pulmonary
744 endothelium reveals widespread metabolic reprogramming. *Pulm Circ* 2: 201–13

745 Flamme I, Oehme F, Ellinghaus P, Jeske M, Keldenich J & Thuss U (2014) Mimicking hypoxia to treat anemia: HIF-
746 stabilizer BAY 85-3934 (Molidustat) stimulates erythropoietin production without hypertensive effects. *PLoS One*
747 9: e111838

748 Gameiro PA, Laviolette LA, Kelleher JK, Iliopoulos O & Stephanopoulos G (2013a) Cofactor balance by
749 nicotinamide nucleotide transhydrogenase (NNT) coordinates reductive carboxylation and glucose catabolism in
750 the tricarboxylic acid (TCA) cycle. *J Biol Chem* 288: 12967–77

751 Gameiro PA, Yang J, Metelo AM, Perez-Carro R, Baker R, Wang Z, Arreola A, Rathmell WK, Olumi A, Lopez-
752 Larrubia P, *et al* (2013b) In vivo HIF-mediated reductive carboxylation is regulated by citrate levels and sensitizes
753 VHL-deficient cells to glutamine deprivation. *Cell Metab* 17: 372–85

754 Garcia-Alonso L, Holland CH, Ibrahim MM, Turei D & Saez-Rodriguez J (2019) Benchmark and integration of
755 resources for the estimation of human transcription factor activities. *Genome Res* 29: 1363–1375

756 Garcia-Bermudez J, Baudrier L, La K, Zhu XG, Fidelin J, Sviderskiy VO, Papagiannakopoulos T, Molina H, Snuderl
757 M, Lewis CA, *et al* (2018) Aspartate is a limiting metabolite for cancer cell proliferation under hypoxia and in
758 tumours. *Nat Cell Biol* 20: 775–781

759 Gardner LB, Li Q, Park MS, Flanagan WM, Semenza GL & Dang CV (2001) Hypoxia inhibits G1/S transition
760 through regulation of p27 expression. *J Biol Chem* 276: 7919–7926

761 Garofalo O, Cox DW & Bachelard HS (1988) Brain levels of NADH and NAD+ under hypoxic and hypoglycaemic
762 conditions in vitro. *J Neurochem* 51: 172–6

763 Gordan JD, Bertout JA, Hu CJ, Diehl JA & Simon MC (2007) HIF-2alpha promotes hypoxic cell proliferation by
764 enhancing c-myc transcriptional activity. *Cancer Cell* 11: 335–47

765 Grassian AR, Parker SJ, Davidson SM, Divakaruni AS, Green CR, Zhang X, Slocum KL, Pu M, Lin F, Vickers C, *et al*
766 (2014) IDH1 mutations alter citric acid cycle metabolism and increase dependence on oxidative mitochondrial
767 metabolism. *Cancer Res* 74: 3317–31

768 Guarino VA, Oldham WM, Loscalzo J & Zhang YY (2019) Reaction rate of pyruvate and hydrogen peroxide:
769 assessing antioxidant capacity of pyruvate under biological conditions. *Sci Rep* 9: 19568

770 Guzy RD, Hoyos B, Robin E, Chen H, Liu L, Mansfield KD, Simon MC, Hammerling U & Schumacker PT (2005)
771 Mitochondrial complex III is required for hypoxia-induced ROS production and cellular oxygen sensing. *Cell*
772 *Metab* 1: 401–8

773 Hubbi ME & Semenza GL (2015) Regulation of cell proliferation by hypoxia-inducible factors. *Am J Physiol Cell*
774 *Physiol* 309: C775–82

775 Hui S, Cowan AJ, Zeng X, Yang L, TeSlaa T, Li X, Bartman C, Zhang Z, Jang C, Wang L, *et al* (2020) Quantitative
776 Fluxomics of Circulating Metabolites. *Cell Metab*

777 Hui S, Ghergurovich JM, Morscher RJ, Jang C, Teng X, Lu W, Esparza LA, Reya T, Le Z, Yanxiang Guo J, *et al* (2017)
778 Glucose feeds the TCA cycle via circulating lactate. *Nature* 551: 115–118

779 Hydbring P, Castell A & Larsson L-G (2017) MYC Modulation around the CDK2/p27/SKP2 Axis. *Genes (Basel)* 8:
780 174

781 Islam MS, Leissing TM, Chowdhury R, Hopkinson RJ & Schofield CJ (2018) 2-Oxoglutarate-Dependent
782 Oxygenases. *Annu Rev Biochem* 87: 585–620

783 Jain IH, Calvo SE, Markhard AL, Skinner OS, To TL, Ast T & Mootha VK (2020) Genetic Screen for Cell Fitness in
784 High or Low Oxygen Highlights Mitochondrial and Lipid Metabolism. *Cell* 181: 716–727 e11

785 Jazmin LJ & Young JD (2013) Isotopically nonstationary 13C metabolic flux analysis. *Methods Mol Biol* 985: 367–
786 90

787 Jiang L, Shestov AA, Swain P, Yang C, Parker SJ, Wang QA, Terada LS, Adams ND, McCabe MT, Pietrak B, *et al*
788 (2016) Reductive carboxylation supports redox homeostasis during anchorage-independent growth. *Nature* 532:
789 255–8

790 Kaelin WG & Ratcliffe PJ (2008) Oxygen sensing by metazoans: the central role of the HIF hydroxylase pathway.
791 *Mol Cell* 30: 393–402

792 Kanehisa M & Goto S (2000) KEGG: kyoto encyclopedia of genes and genomes. *Nucleic Acids Res* 28: 27–30

793 Kim D, Fiske BP, Birsoy K, Freinkman E, Kami K, Possemato RL, Chudnovsky Y, Pacold ME, Chen WW, Cantor JR, *et*
794 *al* (2015) SHMT2 drives glioma cell survival in ischaemia but imposes a dependence on glycine clearance. *Nature*
795 520: 363–7

796 Korotkevich G, Sukhov V, Budin N, Shpak B, Artyomov MN & Sergushichev A (2021) Fast gene set enrichment
797 analysis. 060012 doi:10.1101/060012 [PREPRINT]

798 Koshiji M, Kageyama Y, Pete EA, Horikawa I, Barrett JC & Huang LE (2004) HIF-1alpha induces cell cycle arrest by
799 functionally counteracting Myc. *EMBO J* 23: 1949–1956

800 Koshiji M, To KK-W, Hammer S, Kumamoto K, Harris AL, Modrich P & Huang LE (2005) HIF-1alpha induces
801 genetic instability by transcriptionally downregulating MutSalpha expression. *Mol Cell* 17: 793–803

802 Le A, Lane AN, Hamaker M, Bose S, Gouw A, Barbi J, Tsukamoto T, Rojas CJ, Slusher BS, Zhang H, *et al* (2012)
803 Glucose-independent glutamine metabolism via TCA cycling for proliferation and survival in B cells. *Cell Metab*
804 15: 110–21

805 Lee JW, Ko J, Ju C & Eltzschig HK (2019a) Hypoxia signaling in human diseases and therapeutic targets. *Exp Mol*
806 *Med* 51: 1–13

807 Lee P, Chandel NS & Simon MC (2020) Cellular adaptation to hypoxia through hypoxia inducible factors and
808 beyond. *Nat Rev Mol Cell Biol* 21: 268–283

809 Lee WD, Mukha D, Aizenshtein E & Shlomi T (2019b) Spatial-fluxomics provides a subcellular-compartmentalized
810 view of reductive glutamine metabolism in cancer cells. *Nat Commun* 10: 1351

811 Li F, Wang Y, Zeller KI, Potter JJ, Wonsey DR, O'Donnell KA, Kim J-W, Yustein JT, Lee LA & Dang CV (2005) Myc
812 stimulates nuclearly encoded mitochondrial genes and mitochondrial biogenesis. *Mol Cell Biol* 25: 6225–6234

813 Li H, Meininger CJ, Hawker JR, Haynes TE, Kepka-Lenhart D, Mistry SK, Morris SM & Wu G (2001) Regulatory role
814 of arginase I and II in nitric oxide, polyamine, and proline syntheses in endothelial cells. *American Journal of*
815 *Physiology-Endocrinology and Metabolism* 280: E75–E82

816 Li Y, Sun X-X, Qian DZ & Dai M-S (2020) Molecular Crosstalk Between MYC and HIF in Cancer. *Front Cell Dev Biol*
817 8: 590576

818 Liao Y, Smyth GK & Shi W (2019) The R package Rsubread is easier, faster, cheaper and better for alignment and
819 quantification of RNA sequencing reads. *Nucleic Acids Res* 47: e47

820 Liberzon A, Birger C, Thorvaldsdottir H, Ghandi M, Mesirov JP & Tamayo P (2015) The Molecular Signatures
821 Database (MSigDB) hallmark gene set collection. *Cell Syst* 1: 417–425

822 Liu S-S, Wang H-Y, Tang J-M & Zhou X-M (2013) Hypoxia-induced collagen synthesis of human lung fibroblasts by
823 activating the angiotensin system. *Int J Mol Sci* 14: 24029–24045

824 Long W (2017) Automated amino acid analysis using an Agilent Poroshell HPH-C18 column. *Application Note,*
825 *Agilent Technologies, Inc* Publication Number 5991-5571EN: 1–10

826 Love MI, Huber W & Anders S (2014) Moderated estimation of fold change and dispersion for RNA-seq data with
827 DESeq2. *Genome Biol* 15: 550

828 Madden SK, de Araujo AD, Gerhardt M, Fairlie DP & Mason JM (2021) Taking the Myc out of cancer: toward
829 therapeutic strategies to directly inhibit c-Myc. *Molecular Cancer* 20: 3

830 Mann G, Mora S, Madu G & Adegoke OAJ (2021) Branched-chain Amino Acids: Catabolism in Skeletal Muscle and
831 Implications for Muscle and Whole-body Metabolism. *Front Physiol* 12: 702826

832 Masson N, Keeley TP, Giuntoli B, White MD, Puerta ML, Perata P, Hopkinson RJ, Flashman E, Licausi F & Ratcliffe
833 PJ (2019) Conserved N-terminal cysteine dioxygenases transduce responses to hypoxia in animals and plants.
834 *Science* 365: 65–69

835 Melendez-Rodriguez F, Urrutia AA, Lorendeau D, Rinaldi G, Roche O, Bogurcu-Seidel N, Ortega Muelas M, Mesa-
836 Ciller C, Turiel G, Bouthelier A, *et al* (2019) HIF1alpha Suppresses Tumor Cell Proliferation through Inhibition of
837 Aspartate Biosynthesis. *Cell Rep* 26: 2257–2265 e4

838 Metallo CM, Gameiro PA, Bell EL, Mattaini KR, Yang J, Hiller K, Jewell CM, Johnson ZR, Irvine DJ, Guarente L, *et al*
839 (2011) Reductive glutamine metabolism by IDH1 mediates lipogenesis under hypoxia. *Nature* 481: 380–4

840 Mizuno S, Bogaard HJ, Voelkel NF, Umeda Y, Kadowaki M, Ameshima S, Miyamori I & Ishizaki T (2009) Hypoxia
841 regulates human lung fibroblast proliferation via p53-dependent and -independent pathways. *Respir Res* 10: 17

842 Murphy TA, Dang CV & Young JD (2013) Isotopically nonstationary 13C flux analysis of Myc-induced metabolic
843 reprogramming in B-cells. *Metab Eng* 15: 206–17

844 Murphy TA & Young JD (2013) ETA: robust software for determination of cell specific rates from extracellular
845 time courses. *Biotechnol Bioeng* 110: 1748–58

846 Oldham WM, Clish CB, Yang Y & Loscalzo J (2015) Hypoxia-Mediated Increases in L-2-hydroxyglutarate
847 Coordinate the Metabolic Response to Reductive Stress. *Cell Metab* 22: 291–303

848 Owczarek A, Gieczewska K, Jarzyna R, Jagielski AK, Kiersztan A, Gruza A & Winiarska K (2020) Hypoxia increases
849 the rate of renal gluconeogenesis via hypoxia-inducible factor-1-dependent activation of phosphoenolpyruvate
850 carboxykinase expression. *Biochimie* 171-172: 31–37

851 Pelletier J, Bellot G, Gounon P, Lacas-Gervais S, Pouyssegur J & Mazure NM (2012) Glycogen Synthesis is Induced
852 in Hypoxia by the Hypoxia-Inducible Factor and Promotes Cancer Cell Survival. *Front Oncol* 2: 18

853 Quek LE, Dietmair S, Kromer JO & Nielsen LK (2010) Metabolic flux analysis in mammalian cell culture. *Metab*
854 *Eng* 12: 161–71

855 R Core Team (2022) R: A language and environment for statistical computing Vienna, Austria: R Foundation for
856 Statistical Computing

857 Rabinowitz JD & Enerback S (2020) Lactate: the ugly duckling of energy metabolism. *Nat Metab* 2: 566–571

858 Ritchie ME, Phipson B, Wu D, Hu Y, Law CW, Shi W & Smyth GK (2015) limma powers differential expression
859 analyses for RNA-sequencing and microarray studies. *Nucleic Acids Res* 43: e47

860 Scott DA, Richardson AD, Filipp FV, Knutzen CA, Chiang GG, Ronai ZA, Osterman AL & Smith JW (2011)
861 Comparative metabolic flux profiling of melanoma cell lines: beyond the Warburg effect. *J Biol Chem* 286:
862 42626–34

863 Semenza GL (2012) Hypoxia-inducible factors in physiology and medicine. *Cell* 148: 399–408

864 Sheikh K, Forster J & Nielsen LK (2005) Modeling hybridoma cell metabolism using a generic genome-scale
865 metabolic model of Mus musculus. *Biotechnol Prog* 21: 112–21

866 Stine ZE, Walton ZE, Altman BJ, Hsieh AL & Dang CV (2015) MYC, Metabolism, and Cancer. *Cancer Discov* 5:
867 1024–1039

868 Szoka L, Karna E, Hlebowicz-Sarat K, Karaszewski J & Palka JA (2017) Exogenous proline stimulates type I collagen
869 and HIF-1α expression and the process is attenuated by glutamine in human skin fibroblasts. *Mol Cell Biochem*
870 435: 197–206

871 Tilton WM, Seaman C, Carriero D & Piomelli S (1991) Regulation of glycolysis in the erythrocyte: role of the
872 lactate/pyruvate and NAD/NADH ratios. *J Lab Clin Med* 118: 146–52

873 Vacanti NM, Divakaruni AS, Green CR, Parker SJ, Henry RR, Ciaraldi TP, Murphy AN & Metallo CM (2014)
874 Regulation of substrate utilization by the mitochondrial pyruvate carrier. *Mol Cell* 56: 425–35

875 Vita M & Henriksson M (2006) The Myc oncoprotein as a therapeutic target for human cancer. *Semin Cancer Biol*
876 16: 318–330

877 Wenger RH, Kurtcuoglu V, Scholz CC, Marti HH & Hoogewijs D (2015) Frequently asked questions in hypoxia
878 research. *Hypoxia (Auckl)* 3: 35–43

879 Wheaton WW & Chandel NS (2011) Hypoxia. 2. Hypoxia regulates cellular metabolism. *Am J Physiol Cell Physiol*
880 300: C385–93

881 Wiechert W (2007) The Thermodynamic Meaning of Metabolic Exchange Fluxes. *Biophysical Journal* 93: 2255–
882 2264

883 Wierenga ATJ, Cunningham A, Erdem A, Lopera NV, Brouwers-Vos AZ, Pruis M, Mulder AB, Gunther UL, Martens
884 JHA, Vellenga E, *et al* (2019) HIF1/2-exerted control over glycolytic gene expression is not functionally relevant
885 for glycolysis in human leukemic stem/progenitor cells. *Cancer Metab* 7: 11

886 Wise DR, Ward PS, Shay JE, Cross JR, Gruber JJ, Sachdeva UM, Platt JM, DeMatteo RG, Simon MC & Thompson
887 CB (2011) Hypoxia promotes isocitrate dehydrogenase-dependent carboxylation of alpha-ketoglutarate to
888 citrate to support cell growth and viability. *Proc Natl Acad Sci U S A* 108: 19611–6

889 Xiao W & Loscalzo J (2020) Metabolic Responses to Reductive Stress. *Antioxid Redox Signal* 32: 1330–1347

890 Xue J, Nelin LD & Chen B (2017) Hypoxia induces arginase II expression and increases viable human pulmonary
891 artery smooth muscle cell numbers via AMPKα1 signaling. *American Journal of Physiology-Lung Cellular and*
892 *Molecular Physiology* 312: L568–L578

893 Young JD (2014) INCA: a computational platform for isotopically non-stationary metabolic flux analysis.
894 *Bioinformatics* 30: 1333–5

895 Young JD, Allen DK & Morgan JA (2014) Isotopomer measurement techniques in metabolic flux analysis II: mass
896 spectrometry. *Methods Mol Biol* 1083: 85–108

897 Zamorano F, Wouwer AV & Bastin G (2010) A detailed metabolic flux analysis of an underdetermined network of
898 CHO cells. *J Biotechnol* 150: 497–508

899 Zhang H, Bosch-Marce M, Shimoda LA, Tan YS, Baek JH, Wesley JB, Gonzalez FJ & Semenza GL (2008)
900 Mitochondrial autophagy is an HIF-1-dependent adaptive metabolic response to hypoxia. *J Biol Chem* 283:
901 10892–903

902 Zhang H, Gao P, Fukuda R, Kumar G, Krishnamachary B, Zeller KI, Dang CV & Semenza GL (2007) HIF-1 Inhibits
903 Mitochondrial Biogenesis and Cellular Respiration in VHL-Deficient Renal Cell Carcinoma by Repression of C-MYC
904 Activity. *Cancer Cell* 11: 407–420

905 Zhang J, Sattler M, Tonon G, Grabher C, Lababidi S, Zimmerhackl A, Raab MS, Vallet S, Zhou Y, Cartron M-A, *et al*
906 (2009) Targeting angiogenesis via a c-Myc/hypoxia-inducible factor-1alpha-dependent pathway in multiple
907 myeloma. *Cancer Res* 69: 5082–5090

908

909 **FIGURE LEGENDS**

910 Figure 1: **Effects of hypoxia on extracellular metabolite fluxes in lung fibroblasts.** (**A**) Lung fibroblasts (LFs) were
911 cultured in 21% or 0.5% oxygen beginning 24 h prior to time 0. Samples were collected every 24 h for 72 h. (**B**)
912 Growth curves of LFs in each experimental condition (n = 8). (**C**) Growth rates from (B) were determined by
913 robust linear modeling of log-transformed growth curves. (**D**) Representative immunoblot of LF protein lysates
914 cultured as in (A). (**E**) Relative change in HIF-1α protein levels from (D) normalized to 21% oxygen at time 0 (n =
915 4). (**F**) Relative change in GLUT1 mRNA levels normalized to 21% oxygen treatment at time 0 (n = 4). (**G**) Relative
916 change in LDHA mRNA levels as in (F). (**H**) Relative change in LDHA protein levels as in (E). (**I**) Extracellular fluxes
917 of glucose (GLC) and lactate (LAC) (n = 8). By convention, negative fluxes indicate metabolite consumption. (**J**)
918 Extracellular fluxes of pyruvate (PYR) and amino acids. Data are mean ± SEM (* $p < 0.05$).

919 Figure 2: **Effects of pharmacologic prolyl hydroxylase inhibition on extracellular metabolite fluxes in lung**
920 **fibroblasts.** (**A**) Lung fibroblasts (LFs) were treated with the prolyl hydroxlyase inhibitor molidustat (BAY, 10 μM)
921 or DMSO beginning 24 h prior to time 0. Samples were collected every 24 h for 72 h. (**B**) Growth curves of LFs in
922 each experimental condition (n = 8). (**C**) Growth rates from (B). (**D**) Representative immunoblot of LF protein
923 lysates cultured as in (A). (**E**) Relative change in HIF-1α protein levels from (D) normalized to DMSO at time 0 (n =
924 4). (**F**) Relative change in GLUT1 mRNA levels normalized to DMSO at time 0 (n = 4). (**G**) Relative change in LDHA
925 mRNA levels as in (F). (**H**) Relative change in LDHA protein levels as in (E). (**I**) Extracellular fluxes of glucose (GLC)
926 and lactate (LAC) (n = 8). By convention, negative fluxes indicate metabolite consumption. (**J**) Extracellular fluxes
927 of pyruvate (PYR) and amino acids. Data are mean ± SEM (* $p < 0.05$).

928 Figure 3: **Metabolic flux analysis of lung fibroblasts following hypoxic and pharmacologic PHD inhibition.** (**A**)
929 Mass isotopomer distribution (MID) of pyruvate (PYR) following 72 h labeling with [U-$^{13}C_6$]-glucose (GLC). (**B**)
930 MID of citrate after 72 h labeling with [U-$^{13}C_6$]-GLC (**C**) MID of citrate after 72 h labeling with [U-$^{13}C_5$]-glutamine
931 (GLN). Data are mean ± SEM (n = 4, $p < 0.05$ indicated as * 0.5% *v.* 21% oxygen, † BAY *v.* DMSO, ‡ Δoxygen *v.*
932 ΔBAY). (**D**) Fraction of M5 citrate indicating reductive carboxylation after labeling with [U-$^{13}C_5$]-GLN in LFs and
933 PASMCs (n = 3-4, * $p < 0.05$). (**E**) Ratio of modeled metabolic fluxes in 0.5% oxygen compared to 21% oxygen.
934 Fluxes with non-overlapping confidence intervals are highlighted with arrows colored according to the
935 magnitude of the fold change. Arrow thickness corresponds to the absolute flux measured in hypoxia. (**F**) Ratio
936 of metabolic fluxes in BAY-treated cells compared to DMSO-treated control. Arrows are colored as in (E) and
937 arrow weights correspond to the absolute flux as measured in BAY-treated cells.

938 Figure 4: **PHD inhibition increases lactate uptake and oxidation.** (**A**) Exchange flux estimates for reductive
939 carboxylation of α-ketoglutarate (AKG) to citrate (CIT). Data show the estimate with upper and lower bounds for
940 LFs and PASMCs. (**B**) Exchange flux estimates for lactate import presented as in (A). (**C**) Mass isotopomer
941 distributions of lactate (LAC), fructose-bisphosphate (FBP), pyruvate (PYR), and citrate (CIT) in LFs following 72 h
942 labeling with [U-$^{13}C_3$] lactate. Data are mean ± SEM (n = 4, $p < 0.05$ indicated as * 0.5% *v.* 21% oxygen, † BAY *v.*
943 DMSO, ‡ Δoxygen *v.* ΔBAY).

944 Figure 5: **Metabolomic analysis of molidustat treatment in normoxia and hypoxia.** (**A**) LFs were cultured in
945 standard growth medium and treated with molidustat (BAY, 10 µM) or vehicle (DMSO, 0.1%) in 21% or 0.5%
946 oxygen conditions for 72 h. Growth rates were determined by linear fitting of log-transformed growth curves.
947 (**B**) Glucose uptake in LFs treated with BAY cultured in hypoxia (note reversed *y*-axis). (**C**) Lactate efflux in LFs
948 treated with BAY cultured in hypoxia. Data are mean ± SEM (* $p < 0.05$ BAY *v.* DMSO within a given oxygen
949 exposure). (**D**) Principal component analysis of intracellular metabolites following 72 h of treatment as in (A)
950 suggests a dominant effect of hypoxia over pharmacologic PHD inhibition on the metabolome (n = 7). (**E**)
951 Volcano plot of intracellular metabolites of BAY-treated cells cultured in 21% or 0.5% oxygen. Circles indicate
952 significantly increased (*blue*) and decreased (*red*) levels in hypoxia. (**F**) Metabolite set enrichment analysis of
953 metabolites from (E). All KEGG pathways with p-values < 0.05 are shown. (**G**) Leading edge analysis of the TCA
954 cycle metabolite set. Negative values indicate the relative enrichment associated with BAY treatment compared
955 to hypoxia treatment. Abbreviations: PYR, pyruvate; SUC, succinate; PEP, phosphoenolpyruvate; CIT, citrate;
956 AKG, α-ketoglutarate; MAL, malate; ACO, aconitate; FUM, fumarate. (**H**) NAD^+ from LFs cultured as in (A). (**I**)
957 NADH from LFs cultured as in (A). (**J**) NADH/NAD^+ ratio from (H) and (I). NAD and NADH were determined by
958 enzymatic assay. Data are mean ± SEM (n = 5, $p < 0.05$ with *black* * indicating a significant effect of treatment
959 within a given oxygen tension and *colored* * indicating a significant effect of treatment within a given oxygen
960 tension denoted by the color).

961 Figure 6: **Transcriptomic analysis of molidustat treatment in normoxia and hypoxia.** (**A**) Principal component
962 analysis of transcriptional changes in lung fibroblasts following 72 h of treatment with 0.5% oxygen or
963 molidustat (BAY), separately or together (n = 4). (**B**) Volcano plot illustrating the effects of hypoxia in BAY-
964 treated cells on gene expression. (**C**) Gene set enrichment analysis of transcripts from (B). (**D**) Volcano plot of
965 those transcripts comprising the E2F Targets and G2/M Checkpoint Hallmark gene sets. (**E**) Volcano plot of those
966 transcripts comprising the MYC Targets V1 and V2 Hallmark gene sets. (**F**) Volcano plot illustrating the results of
967 a transcription factor enrichment analysis suggests mechanisms for differential regulation of gene expression
968 following hypoxia or BAY treatment.

969 Figure 7: **MYC regulates HIF-dependent glycolytic flux.** (**A**) Representative immunoblot of MYC protein
970 expression in lung fibroblasts (LFs) following 72 h of treatment with 0.5% oxygen or molidustat (BAY, B). (**B**)
971 Quantification of band densities from (A). (**C**) Working model illustrating that hypoxia-induced MYC antagonizes
972 HIF-dependent metabolic and transcriptional events. (**D**) Representative immunoblot of LFs treated with siRNA
973 targeting MYC (M) demonstrating adequate protein knockdown. (**E**) Growth rates of MYC-knockdown cells
974 cultured in hypoxia. (**F**) Lactate efflux rates of MYC-knockdown cells cultured in hypoxia. (**G**) Representative
975 immunoblot of LFs treated with MYC adenovirus. (**H**) Growth rates of MYC overexpressing cells cultured with
976 BAY. (**I**) Lactate efflux rates of MYC overexpressing cells cultured with BAY. Data are mean ± SEM ($n = 3\text{-}7$, $p <$
977 0.05 as indicated by black * for differences within groups and colored * for differences between groups defined
978 by the *x*-axis).

979

980 **FIGURES**

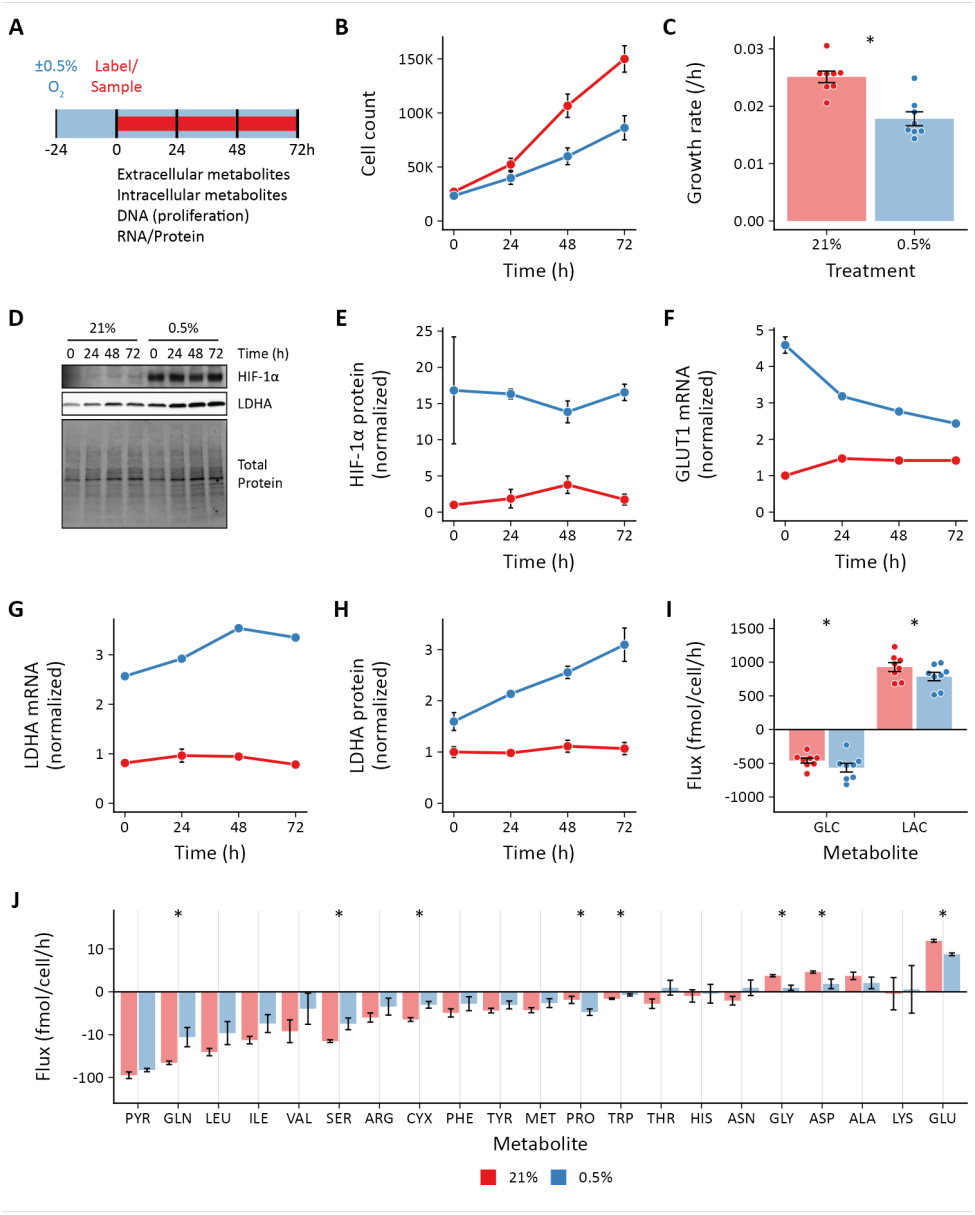

981

982 Figure 1: **Effects of hypoxia on extracellular metabolite fluxes in lung fibroblasts.** (**A**) Lung fibroblasts (LFs) were cultured in 21% or 0.5%
983 oxygen beginning 24 h prior to time 0. Samples were collected every 24 h for 72 h. (**B**) Growth curves of LFs in each experimental
984 condition (n = 8). (**C**) Growth rates from (B) were determined by robust linear modeling of log-transformed growth curves. (**D**)
985 Representative immunoblot of LF protein lysates cultured as in (A). (**E**) Relative change in HIF-1α protein levels from (D) normalized to
986 21% oxygen at time 0 (n = 4). (**F**) Relative change in GLUT1 mRNA levels normalized to 21% oxygen treatment at time 0 (n = 4). (**G**)
987 Relative change in LDHA mRNA levels as in (F). (**H**) Relative change in LDHA protein levels as in (E). (**I**) Extracellular fluxes of glucose (GLC)
988 and lactate (LAC) (n = 8). By convention, negative fluxes indicate metabolite consumption. (**J**) Extracellular fluxes of pyruvate (PYR) and
989 amino acids. Data are mean ± SEM (* $p < 0.05$).

990

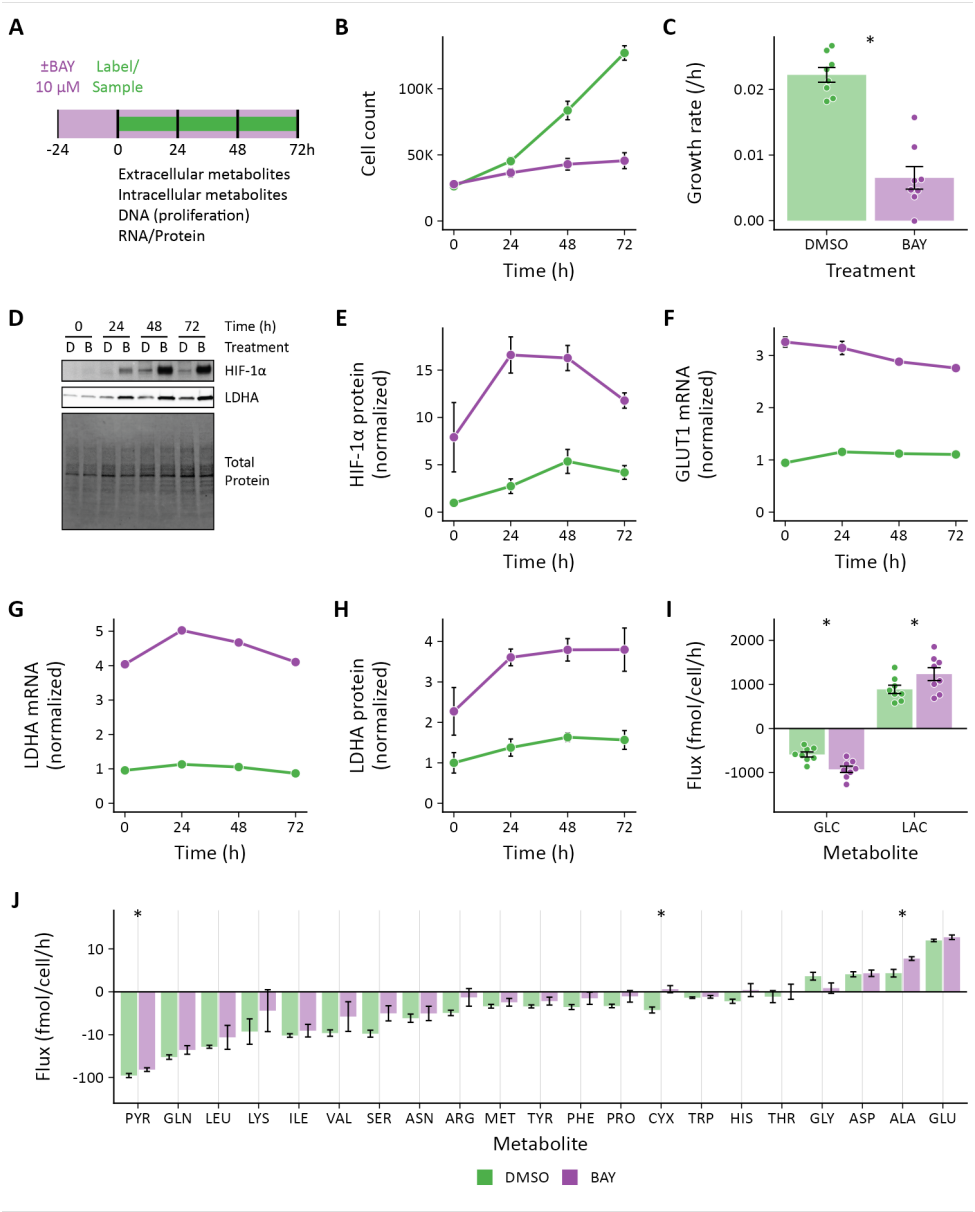

Figure 2: **Effects of pharmacologic prolyl hydroxylase inhibition on extracellular metabolite fluxes in lung fibroblasts.** (**A**) Lung fibroblasts (LFs) were treated with the prolyl hydroxlyase inhibitor molidustat (BAY, 10 µM) or DMSO beginning 24 h prior to time 0. Samples were collected every 24 h for 72 h. (**B**) Growth curves of LFs in each experimental condition (n = 8). (**C**) Growth rates from (B). (**D**) Representative immunoblot of LF protein lysates cultured as in (A). (**E**) Relative change in HIF-1α protein levels from (D) normalized to DMSO at time 0 (n = 4). (**F**) Relative change in GLUT1 mRNA levels normalized to DMSO at time 0 (n = 4). (**G**) Relative change in LDHA mRNA levels as in (F). (**H**) Relative change in LDHA protein levels as in (E). (**I**) Extracellular fluxes of glucose (GLC) and lactate (LAC) (n = 8). By convention, negative fluxes indicate metabolite consumption. (**J**) Extracellular fluxes of pyruvate (PYR) and amino acids. Data are mean ± SEM (* $p < 0.05$).

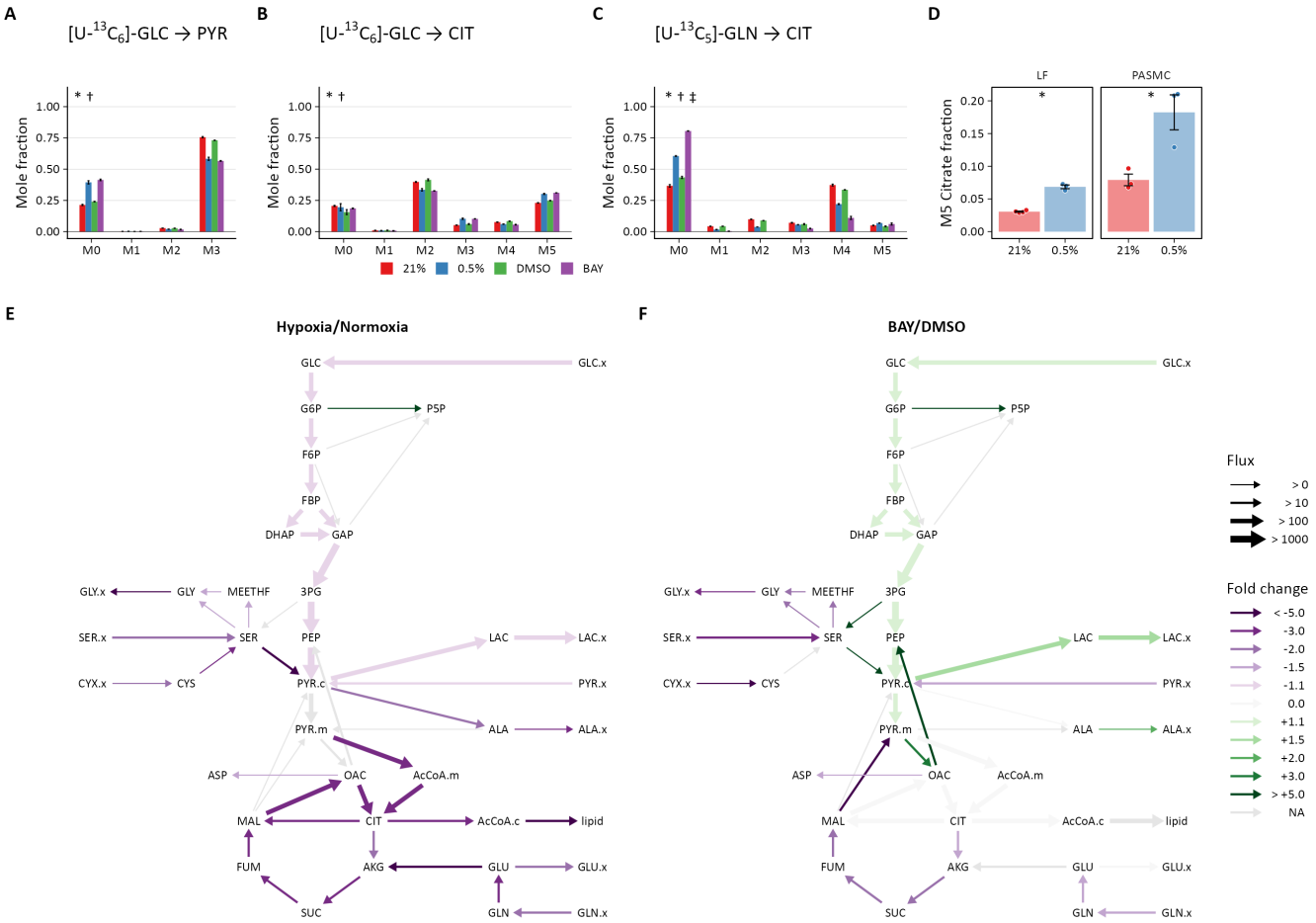

Figure 3: **Metabolic flux analysis of lung fibroblasts following hypoxic and pharmacologic PHD inhibition.** (**A**) Mass isotopomer distribution (MID) of pyruvate (PYR) following 72 h labeling with [U-$^{13}C_6$]-glucose (GLC). (**B**) MID of citrate after 72 h labeling with [U-$^{13}C_6$]-GLC (**C**) MID of citrate after 72 h labeling with [U-$^{13}C_5$]-glutamine (GLN). Data are mean ± SEM (n = 4, $p < 0.05$ indicated as * 0.5% *v.* 21% oxygen, † BAY *v.* DMSO, ‡ Δoxygen *v.* ΔBAY). (**D**) Fraction of M5 citrate indicating reductive carboxylation after labeling with [U-$^{13}C_5$]-GLN in LFs and PASMCs (n = 3-4, * $p < 0.05$). (**E**) Ratio of modeled metabolic fluxes in 0.5% oxygen compared to 21% oxygen. Fluxes with non-overlapping confidence intervals are highlighted with arrows colored according to the magnitude of the fold change. Arrow thickness corresponds to the absolute flux measured in hypoxia. (**F**) Ratio of metabolic fluxes in BAY-treated cells compared to DMSO-treated control. Arrows are colored as in (E) and arrow weights correspond to the absolute flux as measured in BAY-treated cells.

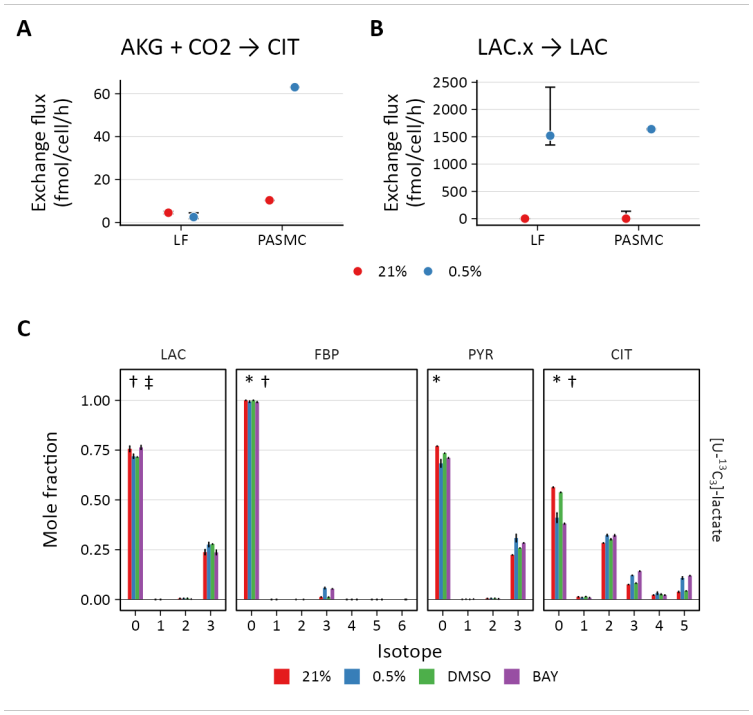

Figure 4: **PHD inhibition increases lactate uptake and oxidation.** (**A**) Exchange flux estimates for reductive carboxylation of α-ketoglutarate (AKG) to citrate (CIT). Data show the estimate with upper and lower bounds for LFs and PASMCs. (**B**) Exchange flux estimates for lactate import presented as in (A). (**C**) Mass isotopomer distributions of lactate (LAC), fructose-bisphosphate (FBP), pyruvate (PYR), and citrate (CIT) in LFs following 72 h labeling with [U-$^{13}C_3$] lactate. Data are mean ± SEM (n = 4, $p < 0.05$ indicated as * 0.5% *v.* 21% oxygen, † BAY *v.* DMSO, ‡ Δoxygen *v.* ΔBAY).

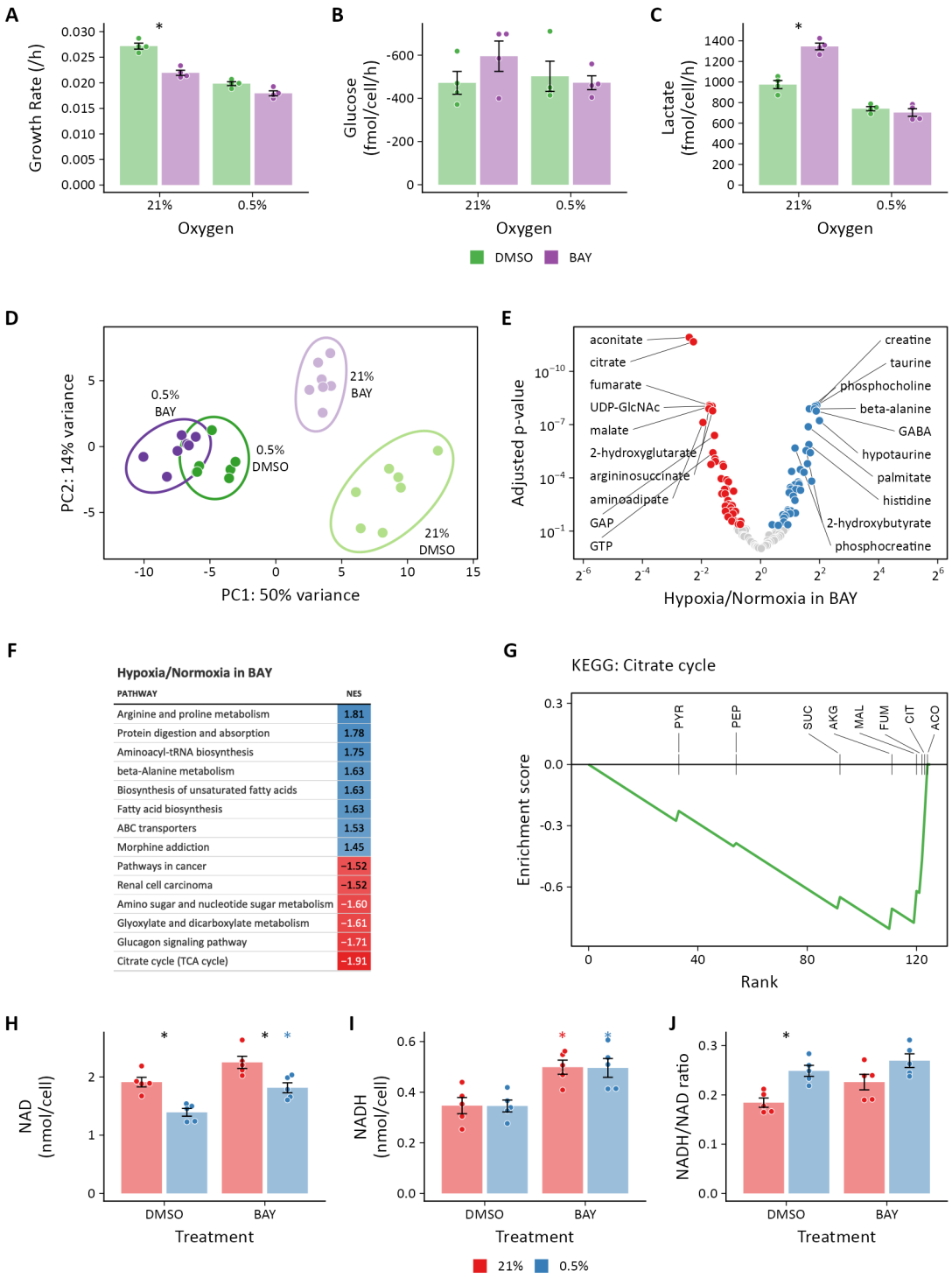

Figure 5: **Metabolomic analysis of molidustat treatment in normoxia and hypoxia.** (**A**) LFs were cultured in standard growth medium and treated with molidustat (BAY, 10 µM) or vehicle (DMSO, 0.1%) in 21% or 0.5% oxygen conditions for 72 h. Growth rates were determined by linear fitting of log-transformed growth curves. (**B**) Glucose uptake in LFs treated with BAY cultured in hypoxia (note reversed *y*-axis). (**C**) Lactate efflux in LFs treated with BAY cultured in hypoxia. Data are mean ± SEM (* $p < 0.05$ BAY *v.* DMSO within a given oxygen exposure). (**D**) Principal component analysis of intracellular metabolites following 72 h of treatment as in (A) suggests a dominant effect of hypoxia over pharmacologic PHD inhibition on the metabolome (n = 7). (**E**) Volcano plot of intracellular metabolites of

1025 BAY-treated cells cultured in 21% or 0.5% oxygen. Circles indicate significantly increased (*blue*) and decreased (*red*) levels in hypoxia. (**F**)
1026 Metabolite set enrichment analysis of metabolites from (E). All KEGG pathways with p-values < 0.05 are shown. (**G**) Leading edge analysis
1027 of the TCA cycle metabolite set. Negative values indicate the relative enrichment associated with BAY treatment compared to hypoxia
1028 treatment. Abbreviations: PYR, pyruvate; SUC, succinate; PEP, phosphoenolpyruvate; CIT, citrate; AKG, α-ketoglutarate; MAL, malate;
1029 ACO, aconitate; FUM, fumarate. (**H**) NAD^+ from LFs cultured as in (A). (**I**) NADH from LFs cultured as in (A). (**J**) NADH/NAD^+ ratio from (H)
1030 and (I). NAD and NADH were determined by enzymatic assay. Data are mean ± SEM (n = 5, p < 0.05 with *black* * indicating a significant
1031 effect of treatment within a given oxygen tension and *colored* * indicating a significant effect of treatment within a given oxygen tension
1032 denoted by the color).

1033

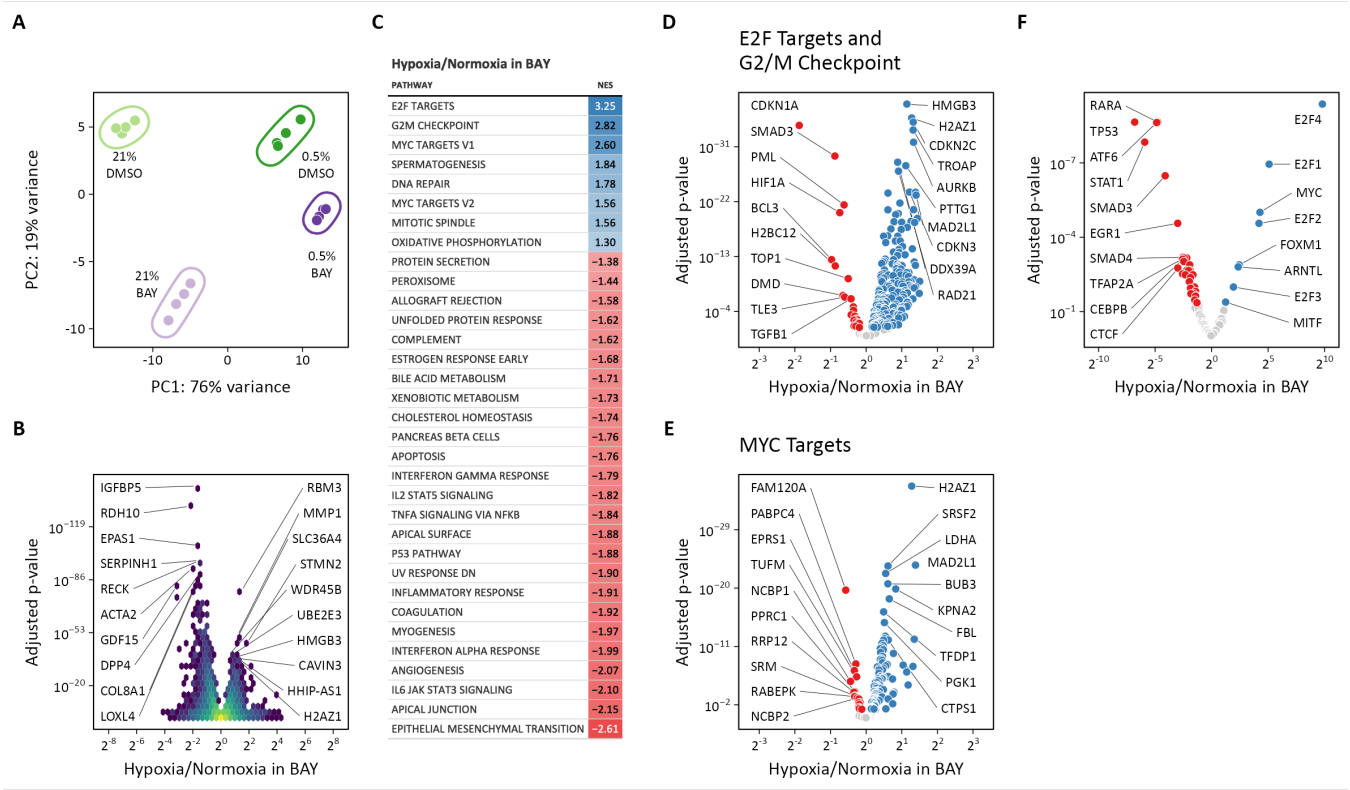

Figure 6: **Transcriptomic analysis of molidustat treatment in normoxia and hypoxia.** (**A**) Principal component analysis of transcriptional changes in lung fibroblasts following 72 h of treatment with 0.5% oxygen or molidustat (BAY), separately or together (n = 4). (**B**) Volcano plot illustrating the effects of hypoxia in BAY-treated cells on gene expression. (**C**) Gene set enrichment analysis of transcripts from (B). (**D**) Volcano plot of those transcripts comprising the E2F Targets and G2/M Checkpoint Hallmark gene sets. (**E**) Volcano plot of those transcripts comprising the MYC Targets V1 and V2 Hallmark gene sets. (**F**) Volcano plot illustrating the results of a transcription factor enrichment analysis suggests mechanisms for differential regulation of gene expression following hypoxia or BAY treatment.

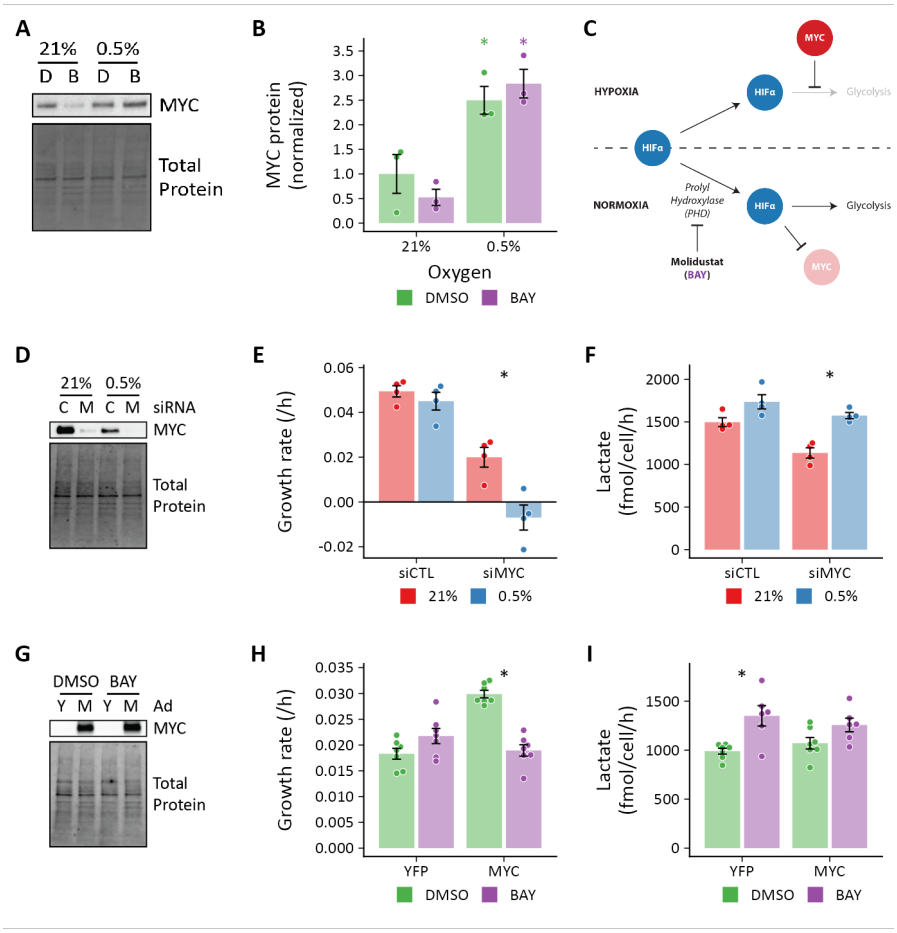

Figure 7: **MYC regulates HIF-dependent glycolytic flux.** (**A**) Representative immunoblot of MYC protein expression in lung fibroblasts (LFs) following 72 h of treatment with 0.5% oxygen or molidustat (BAY, B). (**B**) Quantification of band densities from (A). (**C**) Working model illustrating that hypoxia-induced MYC antagonizes HIF-dependent metabolic and transcriptional events. (**D**) Representative immunoblot of LFs treated with siRNA targeting MYC (M) demonstrating adequate protein knockdown. (**E**) Growth rates of MYC-knockdown cells cultured in hypoxia. (**F**) Lactate efflux rates of MYC-knockdown cells cultured in hypoxia. (**G**) Representative immunoblot of LFs treated with MYC adenovirus. (**H**) Growth rates of MYC overexpressing cells cultured with BAY. (**I**) Lactate efflux rates of MYC overexpressing cells cultured with BAY. Data are mean ± SEM (n = 3-7, $p < 0.05$ as indicated by black * for differences within groups and colored * for differences between groups defined by the *x*-axis).